

Atmospheric turbulence inflow effect on the aerodynamics and aeroacoustics of side-by-side urban air mobility aircraft

M. Sadegh Araghizadeh¹, Bidesh Sengupta², Sang Min Son¹, Hakjin Lee^{1,a}, Rho Shin Myong¹

¹*School of Aerospace Engineering, Gyeongsang National University, Jinju, Gyeongnam 52828, South Korea*

²*Department of Physics and Astronomy, University of Bologna, Bologna 40126, Italy*

^a)Author to whom correspondence should be addressed: hlee@gnu.ac.kr

Abstract

Urban air mobility (UAM) aircraft operate near the planetary surface, exposing them to complex wind conditions in atmospheric turbulence layer. The interaction of atmospheric turbulence with the aircraft significantly impacts its structure as well as its aerodynamic and aeroacoustic performance. This study employs an efficient mid-fidelity aerodynamic method, integrated with the Ffowcs Williams-Hawkings (FW-H) acoustic analogy and a stochastic full-field inflow turbulence generator to investigate the aerodynamic and acoustic performance of side-by-side UAM aircraft while cruising through turbulent inflow. Under uniform wind conditions, aerodynamic loads exhibit steady variations once the rotor wake reaches a converged state. However, as the severity of turbulence increases, the wake structures become increasingly disrupted and eventually deteriorate significantly. Turbulent inflow leads to increased unsteadiness and blade-vortex interactions (BVI), altering both aerodynamic and acoustic characteristics. Higher turbulence level results in elevated sound pressure levels and alteration of acoustic patterns. The impact of inflow turbulence on noise emission is less pronounced in the aft region of the UAM aircraft compared to other directions due to the dominant wake structure propagating downward, mitigating the influence of atmospheric turbulence in that region.

1. Introduction

Technological advancements in electric motors and batteries have boosted the development of hybrid or fully electric vertical takeoff and landing (eVTOL) aircraft using multiple lifting and propelling rotors. Urban air mobility (UAM), a subset of the advanced air mobility concept, comprises technologies that make eVTOL aircraft quieter and more efficient than conventional rotorcraft [1,2] to rapid urbanization and increased fossil fuel consumption in the last decade, governments and industry have worked to develop and certify UAM aircraft prototypes for operation in metropolitan and urban areas as next-generation transportation system [3]. Although eVTOL aircraft has recently been implemented in urban applications [4,5], many challenges and limitations of UAM technologies need to be considered before the large-scale use of eVTOL aircraft can be publicly accepted in highly populated cities.

One of the major concerns regarding the use of UAM aircraft in residential areas is the associated noise pollution [4–7]. Noise generation by UAM aircraft requires standards that differ from those of commercial rotorcraft [8,9]. Accordingly, numerous studies have investigated the acoustic behaviors of different UAM configurations. Jia and Lee [10] and Sagaga and Lee [11,12] implemented a high-fidelity computational fluid dynamics (CFD) solver and the Ffowcs Williams–Hawkings (FW–H) acoustic analogy in PSU-WOPWOP code [13,14] to investigate the aeroacoustic characteristics of NASA (National Aeronautics and Space Administration) side-by-side UAM aircraft with different rotor overlap during cruising and hovering operations. Their simulation results demonstrated that blade–vortex interaction (BVI) is the dominant interaction source in the multirotor eVTOL configuration. Ventura Diaz et al. [15] analyzed the aeroacoustics of NASA’s Quiet Single Main Rotor under hovering and forward flight conditions by loosely coupling high-fidelity CFD with comprehensive rotorcraft code CAMRAD II. Their findings indicated that BVI is weaker in low-noise configurations. Ahuja et al. [16,17] integrated Farassat’s formulation 1A with a surface-vorticity solver to study the propeller configurations of two UAM aircraft—NASA’s X-57 and Joby’s S4 UAM eVTOL. The impacts of various aspects of UAM propeller configuration on noise characteristics have also been further studied recently in Refs. [18–20]. Kim et al. [21] demonstrated that the airframe shape and distance from the rotor system can significantly affect the aeroacoustics of UAM aircraft using a high-fidelity lattice Boltzmann method, the FW-H equation, and a permeable surface. Lee et al. [22] investigated rotor-to-rotor interactional effects on the aerodynamics and aeroacoustics of DJI’s Phantom 2 quadcopter with different rotor

separation distances. Moreover, Yu et al. [23] explored the impact of fixed- and variable-pitch control systems on the aerodynamics and aeroacoustics of multirotor configurations during hovering operations.

Unlike commercial airplanes and conventional helicopters, UAM aircraft operate near the planetary surface and are exposed to severe wind conditions in the planetary boundary layer or atmospheric boundary layer (ABL), the closest atmospheric layer to the Earth's surface. In this layer, wind flow is considerably influenced by terrain or sea surface characteristics, synoptic forcing, and thermal instabilities, causing extreme fluctuations in physical variables such as wind speed, temperature, and humidity (i.e., atmospheric turbulence) [24–26]. Interactions with atmospheric turbulence impact the aircraft structure and its aerodynamic and aeroacoustic performance, increasing operational safety risks and passenger discomfort. Accordingly, modeling atmospheric turbulence and evaluating its impact on aircraft are essential for the development of robust and trustworthy UAM aircraft [27]. Urban environments are aerodynamically complex owing to the clustering of high-rise buildings, which induces turbulent flow and alters local flow conditions. Consequently, realistic atmospheric turbulence inflow must be considered in the aerodynamic and aeroacoustic analysis of UAM aircraft to achieve a more accurate assessment of their performance. However, due to the significant computational and experimental challenges associated with modeling and measuring turbulent inflow, most existing UAM aeroacoustic studies have been conducted under the simplifying assumption of uniform inflow. As a result, there is a clear lack of research that examines the aerodynamic and aeroacoustic performance of full UAM configurations operating in realistic turbulent environments. The present study addresses this gap by systematically analyzing the effects of turbulence inflow on a complete side-by-side rotor configuration.

Wind tunnels are often used to simulate the effects of atmospheric turbulent inflow on aircraft, enabling researchers to realistically model wind conditions by controlling wind flow parameters [28,29]. However, the limitations of wind tunnel testing, such as scalability problems, difficulties in fully modeling the complex characteristics of atmospheric turbulence, and high costs, have prompted researchers to exploit the advantages of numerical methods [30,31]. The large eddy simulation (LES) technique is a prominent numerical method for simulating turbulent flow in the ABL [32,33]. Given that LES is computationally expensive, simulating the ABL using Reynolds-averaged Navier–Stokes (RANS) equations provides a good compromise between accuracy and efficiency. Accordingly, RANS-based approaches combined with two-equation turbulence models are often favored over the LES model when simulating ABL [34–36]. However, owing to the large scale of the ABL and the

considerable computation time required, CFD models are not suitable for the early design stage of UAM aircraft [37–39]. Low-order modeling techniques derived from experimental observations of the isotropic turbulent energy spectrum, such as the von Kármán and Dryden models, are computationally less expensive and faster than many CFD models. Spectral methods, including the power spectral density (PSD) approach, enable statistical analysis of atmospheric turbulence. Owing to their computational efficiency, many turbulence models inspired by the von Kármán model have been developed for real-time simulations of low-altitude flight of UAM aircraft in the ABL [40–42]. In such models, turbulence is generated on a plane in front of the rotorcraft and perpendicular to the flight path, assuming a “frozen field” (Taylor’s hypothesis). The turbulent velocity components are transported backward during the forward flight, forming a three-dimensional (3D) turbulence field. However, the influence of urban structures on flow field conditions makes using the traditional von Kármán model in the urban environment unrealistic [43,44]. The stochastic wind module TurbSim, which was developed by the U.S. Department of Energy’s National Renewable Energy Laboratory (NREL) [45], can produce a full-field flow that includes bursts of coherent turbulence that correspond to eddies in turbulent flow. TurbSim has been widely implemented to generate realistic large-scale coherent turbulent inflow over wind turbines [46–50] and was recently successfully implemented in flight control studies of multirotor aircraft during low-altitude operations [51–54]. Notably, the module is an efficient tool for studying UAM aircraft responses in turbulent inflow during low-altitude operations [55].

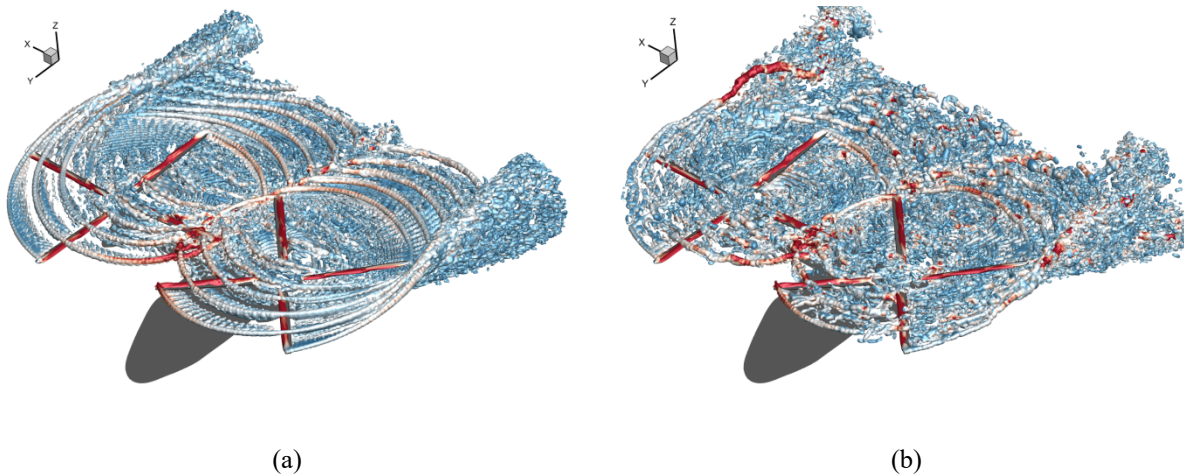


Fig. 1. Effect of atmospheric turbulence on the wake structure of Sbs UAM aircraft under forward flight conditions: (a) without atmospheric turbulence and (b) with atmospheric turbulence at a turbulence intensity of 35%.

Table 1. Detailed review of aerodynamic and aeroacoustic analyses of UAM aircraft

Paper Details	Research details	Inflow condition
Jia and Lee [7] (2022)	Investigating interactional aerodynamics and aeroacoustics of quadrotor UAM configuration using high-fidelity CFD	
Jia and Lee [10] (2020)	Exploring the dominant noise source in SbS rotor configuration and investigating BVI noise generation	
Ahuja et al. [16] (2022)	Flow-acoustic analysis of multiple propeller configurations of UAM aircraft using surface-vorticity solver	
Cantos et al. [18] (2024)	Parametric study of geometric effects on aerodynamics and aeroacoustics of ducted propellers	Uniform inflow
Yu et al. [23] (2024)	Investigating the impact of pitch control systems on aerodynamics and aeroacoustics of multirotor configuration	
Araghizadeh et al. [56] (2024)	Investigating ground effect on aerodynamics and noise level of SbS UAM aircraft	
Present study (2025)	Aerodynamic and aeroacoustic analysis of full-configuration SbS UAM aircraft under turbulent inflow	Turbulent inflow

This study extends our previous work investigating ground effects on the aerodynamic and aeroacoustic performance of NASA’s six-passenger side-by-side (SbS) UAM aircraft during hover operations [56]. This study focuses on forward flight conditions and incorporates atmospheric turbulent inflow, providing a more comprehensive understanding of interactional aerodynamics and aeroacoustics in operational environments. To ensure the safety of UAM operations and enable more accurate noise predictions, the effects of naturally occurring atmospheric turbulence must be considered rather than relying solely on uniform inflow conditions. Fig. 1 depicts the notable impact of atmospheric turbulent inflow on the wake structure of the SbS aircraft. To the best of our knowledge, this is the first study to investigate the impact of atmospheric turbulent inflow on the aerodynamic and aeroacoustic performance of a full-configuration SbS UAM aircraft. Although prior research works on the aeroacoustics of UAM aircraft (See Table 1) have assumed uniform inflow conditions, real urban environments are

inherently unsteady and turbulent. To address this limitation, this study introduces a physically relevant turbulent inflow condition that captures urban atmospheric disturbances for computational analyses of UAM aircraft. To efficiently capture the unsteady aerodynamic and aeroacoustic characteristics of UAM aircraft, this study employs a mid-fidelity numerical framework that models the rotor blades using a nonlinear vortex lattice method (NVLM) and the fuselage using a source-doublet panel approach. The rotor wake field is modeled using the time-accurate vortex particle method (VPM) to efficiently describe the unsteady wake flow. VPM represents the rotor wake as a collection of discrete particles, enabling turbulence-induced variations in the wake structure to be captured over space and time and facilitating a more realistic simulation of wake evolution under turbulent inflow conditions. Rotor noise is evaluated using Farassat's formulation 1A, which provides a solution to the FW-H equation, enabling accurate prediction of thickness and loading noise components radiated from the rotating blades. To maintain computational efficiency, the produced wind disturbances are superimposed onto the aerodynamic model using the disturbance velocity approach (DVA) [57,58]. The findings of the study reveal that turbulent inflow significantly alters aerodynamic forces and noise generation patterns compared to uniform inflow and that unsteady aerodynamic loads and broadband noise levels are strongly affected by turbulence characteristics. Our findings highlight the need to consider realistic atmospheric conditions in the design and certification of UAM aircraft.

2. Numerical Methods

Although high-fidelity CFD methods are well suited to capture complex turbulent flow structures with high accuracy, incorporating turbulent inflow conditions that vary with time and space into a full 3D CFD simulation is typically computationally expensive. Furthermore, the numerical dissipation associated with grid-based solvers can pose challenges in accurately preserving wake structures over long simulation times. To address these limitations, vortex-based methods offer a computationally efficient alternative for modeling unsteady, 3D wake flows. Unlike conventional mesh- or grid-based CFD approaches, vortex-based methods using a Lagrangian formulation do not rely on spatial discretization of the entire flow domain, enabling more accurate tracking of vortical structures with reduced numerical diffusion, especially in wake-dominated flows. Hence, vortex-based methods are particularly well suited for simulating the influence of atmospheric turbulence on rotor wake development in UAM applications. This study employed a coupled vortex method consisting of NVLM, the source-doublet panel method, VPM

integrated with a realistic turbulent simulator, and an aeroacoustic solver to assess the aerodynamic and aeroacoustic performance of SbS eVTOL aircraft. Assuming sufficiently thin rotor blades, NVLM was implemented to simulate the SbS rotor, while the fuselage was represented by source-doublet panels with constant strength, and vortex particles were used to model the wake structures generated by rotor blades. Fig. 2 depicts the flowchart of the coupled vortex method, comprising the aerodynamic solver (NVLM-VPM), the turbulent wind generator (TurbSim), and the aeroacoustic solver based on Farassat’s formulation 1A.

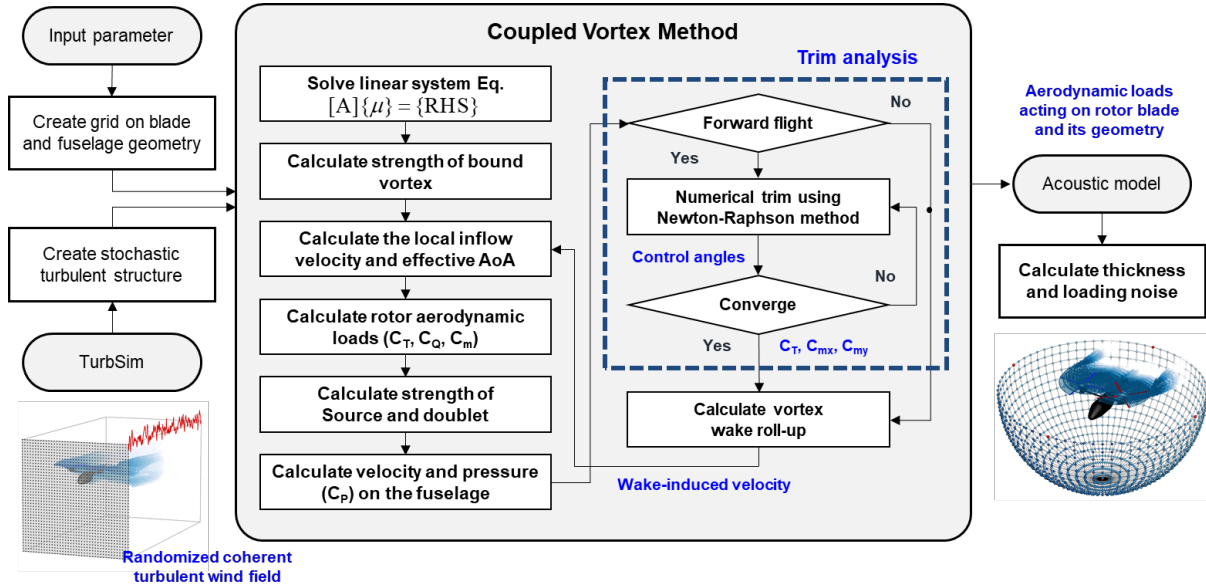


Fig. 2. Flowchart of coupled aerodynamic solver, turbulent wind generator, and aeroacoustic solver for simulating UAM side-by-side aircraft in atmospheric turbulent inflow.

2.1 Aeroacoustic model based on coupled vortex methods

Vortex-based methods assume that flow is inviscid, incompressible, or irrotational. The continuity equation in terms of the velocity potential (ϕ) can be written as a Laplace equation, for which the general solution can be derived using Green’s second identity. Assuming a thin wake surface, the continuity equation is represented by a sum of elementary or single solutions, such as the source (σ) and doublet (μ) distribution on the body surface (S_B) or only μ distribution on the wake surface (S_W). Assuming sufficient thinness, the rotor blade can be regarded as a lifting surface without thickness, nullifying the Laplace equation’s σ term, with only μ distribution remaining. The rotor blades are modeled using vortex ring elements because the constant-strength μ term is equivalent to a

constant-strength vortex ring element with the same strength ($\Gamma = \mu$). Vortex strength is determined by applying no-penetration boundary conditions at each collocation point on discretized vortex ring elements.

Given that rotor simulations inherently involve the unsteady motion of rotor blades, the no-penetration boundary condition must be formulated using the time-dependent kinematic velocity (\mathbf{V}) at each collocation point, as defined by Eq. (1):

$$\mathbf{V} = \mathbf{V}_\infty - \boldsymbol{\Omega} \times \mathbf{r} + \mathbf{V}_{\text{ind,blade}} + \mathbf{V}_{\text{ind,wake}} \quad (1)$$

Here, \mathbf{V} comprises the freestream velocity, the rotational velocity at each collocation point, expressed as $\boldsymbol{\Omega} \times \mathbf{r}$, where $\boldsymbol{\Omega}$ is the angular velocity vector and \mathbf{r} is the position vector of the collocation point relative to the body-fixed frame; and the velocity induced by bound vortices on the rotor blades ($\mathbf{V}_{\text{ind,blade}}$) and wake vortices ($\mathbf{V}_{\text{ind,wake}}$).

In this study, the effect of atmospheric turbulence was incorporated by adding a perturbation velocity induced by turbulence to the freestream velocity term. In previous studies, the freestream velocity has generally been defined as the flight velocity or uniform freestream velocity, and was treated as a constant value in both time and space, even under unsteady simulations. In contrast, the freestream velocity is represented as the sum of the mean velocity ($\mathbf{V}_{\infty,\text{mean}}$) and the perturbation velocity (\mathbf{V}'_∞), where the perturbation component is updated at each time step through interpolation with the unsteady synthetic wind data generated by TurbSim.

$$\mathbf{V}_\infty = \mathbf{V}_{\infty,\text{mean}} + \mathbf{V}'_\infty \quad (2)$$

This formulation ensures that the space- and time-varying inflow turbulence is consistently projected onto all collocation points throughout the simulation domain.

Although conventional VLM effectively models potential flow around lifting surfaces, nonlinear aerodynamic effects such as viscous loss, flow separation, and low Reynolds number (Re) behavior are inherently neglected. To overcome these limitations, NVLM incorporates airfoil lookup tables, semi-empirical aerodynamic models, and vortex strength correction techniques, extending its applicability to a broader range of rotor simulations [59–61]. In NVLM, sectional aerodynamic loads are evaluated using lookup tables as a function of the effective angle of attack (α_{eff}) and Re value evaluated from the time-dependent kinematic velocity at each blade section, as defined by Eq. (3):

$$\alpha_{\text{eff}} = \theta_{\text{twist}} + \theta_{\text{pitch}} - \tan^{-1} \left(\frac{\mathbf{V} \cdot \mathbf{a}_3}{\mathbf{V} \cdot \mathbf{a}_1} \right) \quad (3)$$

where θ_{twist} and θ_{pitch} are the local twist angle and collective pitch angle at each blade section, respectively; and \mathbf{a}_1 and \mathbf{a}_3 are unit vectors along directions tangential and normal to the rotating plane, respectively. Contrary to rotor blades, fuselage thickness cannot be neglected. Accordingly, the source-doublet panel method is implemented to evaluate σ and μ on fuselage and wing panels [62]. The source-doublet panel method is weakly coupled with NVLM, enabling rotor-fuselage and rotor-wing interaction simulations.

It is noted that the aerodynamic formulation adopted in this study is derived under the assumptions of potential flow and therefore does not inherently account for rotational phenomena or dissipative effects associated with turbulence. Consequently, although the influence of atmospheric turbulence is modeled as externally imposed velocity fluctuations, this approach is not capable of fully capturing the effects of spatially distributed turbulence within flow domain, particularly in the determination of singularity strengths on the lifting surfaces. Moreover, the generation, diffusion, and boundary-layer interaction of turbulence near solid surfaces are not inherently considered. Despite these limitations, the vortex-based Lagrangian approach offers distinct advantages in preserving the evolution of wake structures, which is critical for accurately capturing unsteady rotor-wake interactions and their contribution to noise generation.

Lagrangian VPM can accurately simulate the complex wake field of a rotorcraft without the numerical dissipation error caused by volume discretization with the grid. NVLM is tightly integrated with time-accurate VPM to model the wake flow around the SbS rotor. During the time-marching step for wake evolution, each vortex particle is convected away from the rotating rotor blades with a local convection velocity (\mathbf{V}_{conv}) and moves downstream. The convection velocity governing the motion of each vortex particle comprises the freestream velocity (\mathbf{V}_∞), the velocity induced by bound vortices on the rotor blades ($\mathbf{V}_{ind,blade}$) and fuselage panels ($\mathbf{V}_{ind,fuselage}$), and the self-induced velocity from other vortex particles ($\mathbf{V}_{ind,wake}$), as defined by Eq. (4). The velocity component of the i -th vortex particle (x_i) induced by other particles (x_j) can be computed using Eq. (5).

$$\mathbf{V}_{conv}(\mathbf{x}_i, t) = \mathbf{V}_{\infty, mean} + \mathbf{V}'_\infty + \mathbf{V}_{ind, bound} + \mathbf{V}_{ind, fuselage} + \mathbf{V}_{ind, wake} \quad (4)$$

$$\mathbf{V}_{ind, wake}(\mathbf{x}_i, t) = - \sum_{j=1}^S \frac{1}{\sigma_{ij}^3} K(\rho)(\mathbf{x}_i - \mathbf{x}_j) \times \boldsymbol{\alpha}_j \quad (5)$$

where σ_{ij} is a symmetrized smoothing parameter used to conserve linear and angular vortex impulses, ρ is a non-dimensional distance parameter, $K(\rho)$ is the regularized Biot-Savart kernel used for the velocity calculation, and $\boldsymbol{\alpha}_j$ is

the vector-valued total vorticity inside the vortex particle with volume V_j . The convection velocity of each particle is evaluated at each time step, and its position $\mathbf{x}_i(t)$ is updated by solving the convection equation, as expressed in Eq. (6), which uses a second-order Runge–Kutta integration scheme to ensure numerical stability and temporal accuracy:

$$\frac{d}{dt} \mathbf{x}_i(t) = \mathbf{V}_{\text{conv}}(\mathbf{x}_i, t) \quad (6)$$

This process allows the wake to develop over time while accurately capturing unsteady aerodynamic interactions between the blade, fuselage, and wake flow field. The reader may refer to our previous papers [56,63] for a more detailed description of the VPM. Here, the present VPM neglects the viscous diffusion of vorticity, which may influence the long-term evolution and attenuation of wake structures in the far wake. However, the primary focus of this study is on near-wake dynamics, which dominate rotor aerodynamic loads and noise generation. In this regime, vorticity advection is much stronger than viscous diffusion, and the influence of wake dissipation occurring farther downstream is comparatively minor. Vorticity diffusion models such as particle strength exchange or core spreading will be incorporated in future work to enhance the physical fidelity of the wake simulation.

The current study primarily focuses on predicting the loading noise component generated by unsteady aerodynamic forces acting on SbS rotor blades due to turbulent inflow. This component, while induced by stochastic turbulence, is treated as a deterministic aeroacoustic response within the framework of the aeroacoustic model. Other non-deterministic noise mechanisms, such as turbulence ingestion noise and airfoil self-noise, are not modeled in the current simulation. The airfoil self-noise, including trailing edge (TE) noise, and turbulence ingestion (TI) noise can contribute to the overall acoustic signature of rotor systems under certain operating conditions. For airfoil self-noise, TE noise is a dominant mechanism and may manifest as tonal noise under low Reynolds number conditions due to laminar boundary layers through mechanisms such as vortex shedding or Tollmien–Schlichting (TS) waves, or as broadband noise under higher Reynolds number conditions due to turbulent boundary layers. Predicting these contributions requires resolving boundary-layer flow over the blade surface or implementing semi-empirical models, which are beyond the scope of the present mid-fidelity approach. Although these additional noise sources may influence the spectral results and directivity patterns, their impact is expected to be secondary for the SbS UAM configuration and operating conditions considered in this study, where loading noise is the dominant contributor in the low- and mid-frequency ranges. In this study, thickness and loading noise SPLs are evaluated

through the numerical implementation of Farassat's formulation 1A, a solution to the FW-H equation that neglects the quadrupole source term [14,64] that provides an integral method for evaluating aerodynamically generated noise. The total acoustic pressure is obtained through summing up the thickness and loading noise, which are modeled using surface sources in terms of monopole and dipole sources [22].

2.2 Atmospheric turbulence model

The inflow turbulence fields used in this study were generated using TurbSim, a stochastic, full-field, turbulence generator [65,66], which provides synthetic turbulent fluctuations representative of atmospheric conditions. However, this method does not account for turbulence generation or modification near solid surfaces such as the rotor blades and fuselage. In the present study, our primary focus is on quantifying the effects of externally imposed inflow unsteadiness, rather than wall-induced turbulence, on rotor aerodynamics, wake dynamics, and noise generation. This modeling approach enables a systematic investigation of the effects of turbulence intensity and mean wind speed, within a computationally efficient framework suitable for parametric studies. This module has been proven to be an efficient tool for studying UAM aircraft responses through low-frequency turbulence inflow in low-altitude [55]. In this study, the generated turbulent components are described by the von Kármán spectrum, adopting a wind shear with a power law of exponent 0.3 for urban areas where at least 15% of the area is covered by buildings with an average height of 15 m [67]. The von Kármán model employs irrational functions, offering an accurate spectral description [43, 68, 69]. It provides a more realistic representation of atmospheric turbulence in low-altitude, complex flow environments and has shown better agreement with experimental data, particularly at higher spatial frequencies [41].

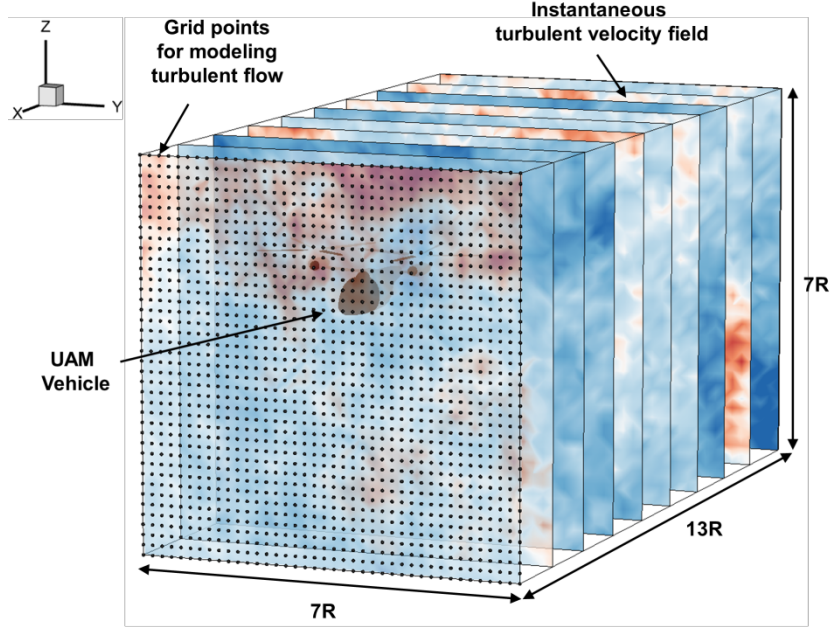


Fig. 3. The atmospheric turbulence field generated by the turbulence simulator (only some velocity planar fields are demonstrated for clarity. Higher velocity regions are visualized in red, while lower velocity regions appear in blue.).

Fig. 3 shows the atmospheric turbulence field represented as a control volume covering the SbS UAM aircraft and its propagated wake during flight. The longitudinal direction of the turbulence field is along the airspeed of the UAM aircraft. The front surface is in front of the main rotor and perpendicular to the airspeed. The size of the turbulence domain field is based on the radius of the main rotor (R). The filters related to the spatial correlation of the von Kármán model are distributed over the front surface. Random numbers generated by a pseudorandom number generator are used to create random phases (one per frequency per grid point per wind component) for the velocity time series. The spectra of the velocity components and spatial coherence are defined in the frequency domain. The frequency spectrum of the longitudinal wind component in the von Kármán model is expressed as follows:

$$S_u(f) = \frac{4\sigma_u^2 L / U_{hub}}{\left[1 + 71(fL / U_{hub})^2\right]^{5/6}} \quad (7)$$

and the lateral ($k = v$) and vertical ($k = w$) components of the wind are defined as follows:

$$S_k(f) = \frac{2\sigma_k^2 L / U_{hub}}{\left[1 + 71(fL / U_{hub})^2\right]^{1/6}} \left[1 + 189(fL / U_{hub})^2\right] \quad (8)$$

where L is defined using the turbulence scale parameter. The spatial coherence function, which describes the correlation of the same wind components of spatially separated points, is calculated as follows:

$$Coh_{i,j} = \exp \left[-12 \sqrt{\left(\frac{f r_{i,j}}{U_{hub}} \right)^2 + \left(0.12 \frac{r_{i,j}}{L_c} \right)^2} \right] \quad (9)$$

where f is the frequency, r_{ij} is the distance between points i and j , and L_c is the coherence scale parameter for the mean wind direction. Once the spectra of the velocity components and spatial coherence are defined in the frequency domain, an inverse Fourier transform produces the time series of three-component wind-speed vectors at grid points. More details on the TurbSim methodology could be sought in Refs. [45,47,70].

To incorporate realistic turbulent inflow conditions into the vortex-based simulation framework, the following five-step procedure is implemented:

- (1) A synthetic turbulent wind field is generated using TurbSim, which constructs 3D stochastic velocity components over a spatial grid aligned with the mean wind direction (along the x -direction). The turbulent field is resolved at discrete grid points, capturing time- and space-varying wind disturbances relevant to UAM operations, as shown in Fig. 3.
- (2) To reconstruct the local unsteady wind field across rotor and wake domains, Taylor's frozen turbulence hypothesis is employed, in which eddies in turbulent flow are convected downstream at the mean wind speed while preserving their spatial structure and spectral characteristics [71]. This assumption has been shown to be valid for low-altitude, low-speed operations ($\mu < 0.3$) [72–74].
- (3) The coupled vortex method operates entirely within a Lagrangian framework and requires only surface discretization, offering important advantages in terms of computational efficiency and wake preservation. By convecting discrete vortices or vorticity-carrying particles without relying on a volumetric mesh, the method minimizes the numerical dissipation that typically arises in Eulerian grid-based CFD solvers. This enables accurate tracking of trailing wake structures—such as tip vortices and inter-rotor wake interaction—over extended durations and distances with minimal degradation. However, an efficient spatial mapping is necessary to apply the volumetrically defined turbulent inflow to surface-based vortex elements (e.g., collocation points on rotor blades and fuselage, wake particles). For this purpose, a K-D tree-

partitioning algorithm is utilized to identify the nearest turbulence grid points to each computational element [61].

- (4) The local turbulent velocity at each collocation point and wake particle is obtained via nearest-neighbor interpolation from the grid nodes defined by TurbSim. This interpolation enables the time- and space-varying turbulence field to be accurately projected onto the vortex elements, ensuring that each computational point receives an appropriate disturbance velocity that reflects its location and time step.
- (5) Finally, the interpolated turbulence velocities are superimposed onto the freestream velocity using DVA [57,58]. Although existing vortex methods typically assume a spatially and temporally uniform freestream velocity, the velocity field in this study is updated at every time step by incorporating unsteady turbulence effects.

Consequently, the freestream velocity is no longer treated as a constant vector but instead varies both spatially and temporally due to the influence of atmospheric turbulence. The time-dependent kinematic velocity used to evaluate the aerodynamic loads acting on rotor blades, as defined by Eq. (1), and the convection velocity of the vortex particles used for wake evolution, as defined by Eq. (4), are redefined to include the local turbulence fluctuation components u' , v' , and w' in the x (longitudinal)-, y (lateral)-, and z (vertical)-directions, respectively, where the x -axis corresponds to the forward flight direction of the UAM aircraft. The turbulence field alters the spatial distribution of wake particles, modifying mutual induction effects among particles. These changes ultimately lead to considerable variations in the resulting wake structure and its aerodynamic influence (Fig. 1).

3. Numerical Setup

3.1 NASA side-by-side UAM model and computational grid

The aircraft prototype used in this study is a publicly available NASA OpenVSP model of a SbS UAM aircraft [75], omitting the landing gear and strakes. The SbS eVTOL aircraft is a representative high-performance rotorcraft comprising two rotors that interact aerodynamically because they physically overlap and intermesh. Interaction between the main rotors is intended to reduce the induced power during forward flight. Further details of this aircraft can be found elsewhere [76,77]. Herein, the relative rotor phasing is held constant, and the phase shift between rotors is 45° . The separation distance (d), defined as the distance between the hubs of two rotors, corresponds to 85%

of the radius of the rotor ($d/R = 0.85$). Overlapping rotors are more efficient during cruising operations than isolated rotors, and the best setup is 15% rotor overlap, which is the overlapped distance scaled by the rotor radius. The hub-to-hub separation distance is $1.7R$ [12]. The rotors are articulated with four blades per rotor and controlled via collective and cyclic pitch angles. Given that the material properties of the conceptual designs were not available, the rotor blades are assumed to be rigid. The rotor blades are modeled based on two modern airfoils: Boeing’s VR-12 and Sikorsky’s SSC-A09. VR-12 is used for an $r/R < 85\%$ span, a linear interpolation between VR-12 and SSC-A09 is assumed to range from 85% to 95%, and SSC-A09 is used for an $r/R > 95\%$ span. The chord length of the blade is 0.217 m until $r/R = 94\%$, at which point the blade tapers. The slope of the linear twist distribution is assumed to be -16° , and 0° twist occurs at a 75% span. A 15° linear taper ratio is applied between $r/R = 94\%$ and the blade tip. The fundamental specifications of these aircraft are listed in Table 2.

Table 2. Parameters of NASA’s SbS eVTOL aircraft

Parameter	Value
Overlap ratio [%]	15
Number of rotors [-]	2
Number of blades [-]	4
Rotor radius, R [m]	3.203
Rotor solidity, σ [-]	0.0832
Gross weight, W [kg]	1792
Tip Mach number, M_{tip} [-]	0.484

The computational grid system comprises the fuselage, engine cowling, tail wing, and rotor blades without hubs. A grid sensitivity study was performed by refining the total number of chordwise and spanwise lattices on the rotor blades, resulting in a mesh refinement factor of approximately 1.3 for the total number of cells between successive grids. The coarse, medium, and fine grids consisted of 10,748, 14,948, and 19,108 cells, respectively. The average thrust coefficient at the last revolution was evaluated for each case, and the relative deviation $|\Delta C_T/C_T|$ was 3% between the coarse and medium grids, and less than 1% between the medium and fine grids. Based on this analysis, the medium grid was selected for the present simulations, in which each rotor blade is discretized with 720

quadrilateral vortex lattices and the fuselage, engine cowling, and tail wing are represented by 9,188 unstructured triangular source–doublet panels. The surface grids for the numerical simulation of the SbS aircraft are depicted in Fig. 4. As you can see in this figure, the rotor on the starboard side (highlighted in blue) rotates counterclockwise (CCW), and the rotor on the port side (highlighted in red) rotates clockwise (CW). The rotor azimuth angle (ψ_R) is defined in relation to the CCW rotation of the starboard side rotor, while the microphone azimuth angle (ψ_{MIC}) is defined based on the longitudinal axis of aircraft, measured CCW rotation from the rear of the aircraft (See Fig. 4). The azimuth angle of the microphones (ψ_{MIC}) aligns with the rotor azimuth angle (ψ_R). For the aeroacoustic analysis, a total of 36 microphones are uniformly distributed in a circular array around the aircraft, located 50 m radially (approximately 16R) and 50 m vertically below the rotor system. The microphones are spaced every 10° in azimuth, and the acoustic data at each observer location is post-processed to assess directivity and tonal noise characteristics during rotor operation.

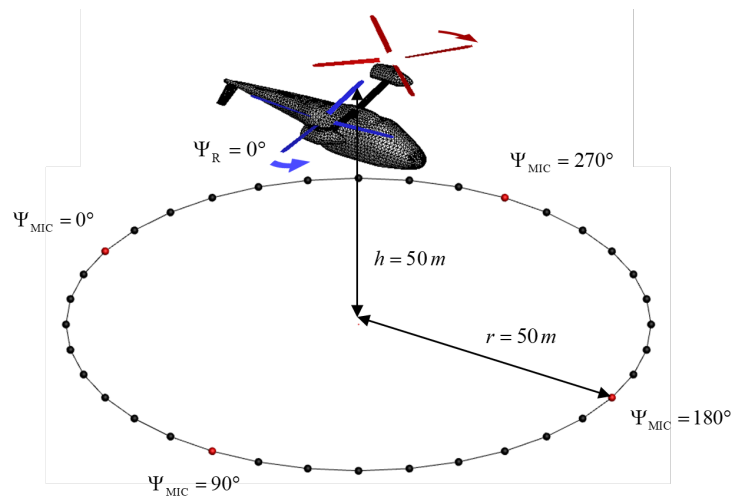


Fig. 4. Surface grid of SbS UAM aircraft with 15% rotor overlap, azimuth angles, and microphone locations (not drawn to scale).

Three different time-step sizes were evaluated to assess their influence on the solution. The largest, medium, and smallest time steps corresponded to azimuthal increments of 8° , 4° , and 3° per time step, respectively. The relative deviation in the thrust coefficient $|\Delta C_T/C_T|$ between the largest and medium time steps was 0.8%, while the deviation between the medium and smallest time steps was 0.3%. This indicates that the time step of 4° is sufficiently small to resolve the unsteady load characteristics without introducing excessive numerical smoothing, thus meeting the accuracy requirements of the present study. In this study, a time step of 4° azimuthal increment per

step was adopted for all unsteady simulations. Each simulation was run for 10 full rotor revolutions to allow for sufficient wake development and reliable acoustic signal extraction.

3.2 Trim analysis for SbS rotor system

In this study, the SbS aircraft is assumed to be cruising at a relatively moderate advance ratio (μ) of 0.15. Unlike during hovering and vertical flight, the rotor blade under forward flight conditions experiences asymmetric aerodynamics as the blade rotates with respect to the flight direction. The advancing blade has a higher velocity relative to the air than its rotational velocity, whereas the retreating blade has a lower velocity relative to the air. This lateral asymmetry has a major influence on the rotor in forward flight [78]. Here, we introduce a trim analysis for SbS rotorcraft, similar to the trim analysis used in previous studies [10,77]. The rotor collective trims the total thrust of the two rotors to balance the weight of the aircraft, and each rotor is trimmed to have zero flapping due to lateral and longitudinal cyclic pitches [76,79]. The rotor shaft tilt angle trims the propulsive force of the rotorcraft. In our analysis, the yawing moment and lateral force were not trimmed (they were close to zero due to the symmetrical configuration of aircraft).

The feathering motions of the right and left rotors are described by the following first harmonic functions:

$$\theta_{75}^R = \theta_0^R + \theta_{1c}^R \cos \psi(t) + \theta_{1s}^R \sin \psi(t) \quad (10)$$

$$\theta_{75}^L = \theta_0^L + \theta_{1c}^L \cos \psi(t) + \theta_{1s}^L \sin \psi(t) \quad (11)$$

In the trimming analysis, we aimed to find the roots of the following equation:

$$F(\mathbf{x}) = f(\mathbf{x}) - f_{\text{target}} = 0 \quad (12)$$

The modified Newton–Raphson method is implemented to enhance solution convergence stability:

$$\Delta \mathbf{x} = \mathbf{x}_{n+1} - \mathbf{x}_n = -\lambda [\mathbf{A}]^{-1} \Delta \mathbf{f} \quad (13)$$

where λ is a relaxation factor that changes based on the convergence rate of the response. The input vector elements represent the correction values applied to the blade pitch angles of each rotor in the next calculation step. The response vector elements correspond to the difference between the target trim values and aerodynamic loads obtained from the simulation in one rotor revolution, as defined by Eq. (14):

$$\Delta \mathbf{x} = \begin{bmatrix} \Delta \theta_0^R \\ \Delta \theta_{1x}^R \\ \Delta \theta_{1c}^R \\ \Delta \theta_0^L \\ \Delta \theta_{1x}^L \\ \Delta \theta_{1c}^L \\ \Delta \theta_{nb} \end{bmatrix}, \Delta \mathbf{f} = \begin{bmatrix} \Delta C_{F_z}^R = C_{F_z, target}^R - C_{F_z}^R \\ \Delta C_{M_y}^R = C_{M_y, target}^R - C_{M_y}^R \\ \Delta C_{M_x}^R = C_{M_x, target}^R - C_{M_x}^R \\ \Delta C_{F_z}^L = C_{F_z, target}^L - C_{F_z}^L \\ \Delta C_{M_y}^L = C_{M_y, target}^L - C_{M_y}^L \\ \Delta C_{M_x}^L = C_{M_x, target}^L - C_{M_x}^L \\ \Delta C_{F_z} = C_{F_z, target} - C_{F_z} \end{bmatrix} \quad (14)$$

The coefficient matrix A is constructed with the partial derivatives of the trim condition variables to the blade pitch angles, as defined by Eq. (15):

$$\mathbf{A} = \begin{bmatrix} \frac{\partial C_{F_z}^R}{\partial \theta_0^R} & 0 & 0 & 0 & 0 & 0 & 0 \\ 0 & \frac{\partial C_{M_y}^R}{\partial \theta_{1x}^R} & \frac{\partial C_{M_y}^R}{\partial \theta_{1c}^R} & 0 & 0 & 0 & 0 \\ 0 & \frac{\partial C_{M_x}^R}{\partial \theta_{1x}^R} & \frac{\partial C_{M_x}^R}{\partial \theta_{1c}^R} & 0 & 0 & 0 & 0 \\ 0 & 0 & 0 & \frac{\partial C_{F_z}^L}{\partial \theta_0^L} & 0 & 0 & 0 \\ 0 & 0 & 0 & 0 & \frac{\partial C_{M_y}^L}{\partial \theta_{1x}^L} & \frac{\partial C_{M_y}^L}{\partial \theta_{1c}^L} & 0 \\ 0 & 0 & 0 & 0 & \frac{\partial C_{M_x}^L}{\partial \theta_{1x}^L} & \frac{\partial C_{M_x}^L}{\partial \theta_{1c}^L} & 0 \\ 0 & 0 & 0 & 0 & 0 & 0 & \frac{\partial C_{F_z}}{\partial \theta_{nb}} \end{bmatrix} \quad (15)$$

The wing of SbS rotor system is a faired structure that does not generate lift [80]. The total lift produced by the rotor system is greater than the gross weight of the SbS UAM aircraft, and the parasite drag in forward flight is assumed to be expressed by the equivalent flat plate area. This drag component can be calculated using the standard drag formula [81]:

$$D_0 = \frac{1}{2} \times \rho \times V^2 \times f_e \quad (16)$$

where f_e is the equivalent flat plate area, which for an SbS aircraft with electric propulsion is reported to be 7.5 square feet [82,83]. The rotational speed and pilot input for all cases were constant. The final values of the rotor system tilt

angle (θ_{tilt}), coning angle (β_0), starboard and port rotor collective pitch (θ_0), lateral cyclic pitch (θ_{1c}), and longitudinal cyclic pitch (θ_{1s}) when cruising through a clear atmosphere (without turbulence) are listed in Table 3. Trim analysis is performed under nonturbulent conditions to determine the control angles, and these trimmed blade settings are then applied to all cases involving atmospheric turbulence.

Table 3. Converged pilot inputs of SbS rotor system.

Parameter	Starboard side	Port side
Coning angle, β_0 [°]		3.1
Tilt angle, θ_{tilt} [°]		-0.49
Collective pitch angle, θ_0 [°]	7.31	7.34
Lateral cyclic pitch angle, θ_{1c} [°]	-3.50	-1.70
Longitudinal cyclic pitch angle, θ_{1s} [°]	-3.29	-2.90

3.3 Atmospheric turbulence conditions

The ABL can have a depth of tens of meters to up to a few kilometers. The disturbed air volume between roughness elements, which may refer to crop fields, forests, or urban areas, is called the canopy layer. The vertical wind profile takes an exponential form in this layer; however, the profile depends on the geometry of the roughness elements and cannot be generally described [25,26]. Therefore, the environment in which UAM aircraft operate often experiences turbulence and wind shear. In this study, atmospheric turbulence is characterized by varying the mean wind speed (V_{wind}) and turbulence intensity (TI) based on turbulence observations in urban areas [26,84,85]. with higher TI values observed closer to the ground and a wide range of horizontal velocities observed in complex environments. Accordingly, six atmospheric turbulence cases are considered to explore the impact of wind speed and TI on rotor aerodynamics, wake structures, and noise levels (Table 4). It is noted that turbulence intensity generally decreases with increasing wind speed in realistic atmospheric environments. However, the inflow conditions in this study were deliberately designed to decouple these parameters to systematically analyze the independent effects of mean wind speed and turbulence intensity. This allows for clearer identification of their respective influences on aerodynamic loads and noise generation of the UAM aircraft. To enable a comparative analysis across all six simulation cases, the forward flight speed of the UAM aircraft is adjusted according to V_{wind} , ensuring that the resulting total velocity experienced by the UAM aircraft remains constant at 48 knots (24.69 m/s). Case 1

represents the operation of the aircraft in a clear atmosphere with $\mu = 0.15$. In cases 2–4, V_{wind} in the flight direction is fixed at 10 knots (5.14 m/s) while the TI values increase. In cases 4–6, the V_{wind} values increase although the TI value remains constant (35%), resulting in larger eddy magnitudes.

Table 4 summarizes the case matrix for assessing the impact of atmospheric turbulence. As turbulence severity increases, the inflow turbulent kinetic energy (TKE) also rises accordingly. In this table, the reported TKE represents the mean ideal value under the assumption of isotropic turbulence, computed as [86]:

$$\text{TKE}_{\text{ideal}} = \frac{3}{2} (TI \times V_{\text{wind}})^2 \quad (17)$$

The ideal TKE assumed an isotropic turbulence condition. However, the maximum instantaneous turbulent kinetic energy (TKE) and coherent turbulence kinetic energy (CTKE) reported by TurbSim are expectedly higher than this value [65].

Table 4. Summary of test cases for atmospheric turbulence impact

Case	Total velocity [knot]	Forward flight velocity [knot]	Mean wind velocity [knot]	Turbulence intensity (TI) [%]	Ideal turbulent kinetic energy ($\text{TKE}_{\text{ideal}}$) [m^2/s^2]
1		48	0	0	-
2		38	10	15	0.89
3		38	10	25	2.48
4	48	38	10	35	4.86
5		28	20	35	19.45
6		18	30	35	43.77

The freestream velocity vector (\mathbf{V}_{∞}) used in the coupled vortex method and VPM, defined by Eq. (2) is replaced by the total velocity ($\mathbf{V}_{\text{total}}$), which comprises the forward flight velocity of the UAM aircraft ($\mathbf{V}_{\text{forward}}$), mean wind speed (\mathbf{V}_{wind}), and turbulence fluctuation components (\mathbf{V}'_{∞}), as defined by Eq. (18):

$$\mathbf{V}_{\text{total}}(x, y, z, t) = \mathbf{V}_{\text{forward}} + \mathbf{V}_{\text{wind}} + \mathbf{V}'_{\infty}(x, y, z, t) \quad (18)$$

The forward flight and mean wind velocities are aligned with the x -axis direction, whereas the turbulence fluctuation components are considered in the x -, y -, and z -axis directions. By employing this formulation, the total

velocity component experienced by the UAM aircraft is updated at each time step for all computational elements, including vortex lattices, source-doublet panels, and vortex particles, based on the wind field dataset generated by the turbulent wind generator. The proposed simulation framework captures time- and space-varying inflow conditions with improved physical fidelity, which is essential for accurately modeling turbulence effects on rotor aerodynamics and wake development.

Fig. 5 shows the turbulent inflow field applied to the UAM simulation. The turbulence field is defined over a discretized spatial domain and provides directionally resolved fluctuations in all three Cartesian components (x , y , and z) to model realistic atmospheric disturbances encountered during forward flight. The initial wind data are computed at a temporal resolution of 0.017 s. To match the finer time step required by the unsteady aerodynamic solver (0.0014 s), a linear temporal interpolation kernel is applied to reconstruct intermediate wind velocity values at each collocation and vortex particle location. This interpolation ensures consistent temporal resolution between the turbulence input and vortex-based aerodynamic computations, allowing for accurate representation of time-varying inflow disturbances.

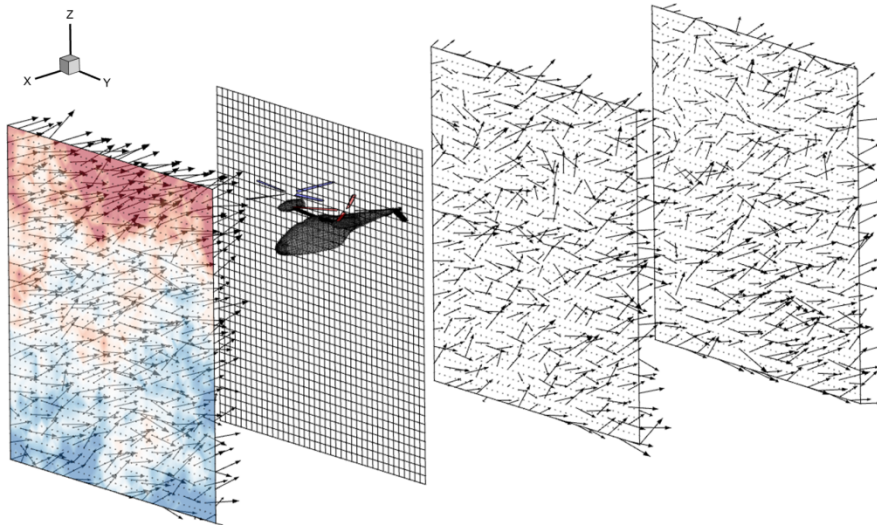


Fig. 5. Turbulent inflow field with time- and space-varying velocities, structured grid for synthetic turbulence generation, and fluctuation vectors in all three directions. (Higher velocity regions are visualized in red, while lower velocity regions appear in blue.)

Fig. 6 shows samples of the time histories of turbulent wind velocity generated by TurbSim for 10 min, from which the velocity profiles are extracted considering computational time constraints, with cases 1 and 6 possessing the minimum and maximum values of the turbulent wind velocity fluctuation components, respectively.

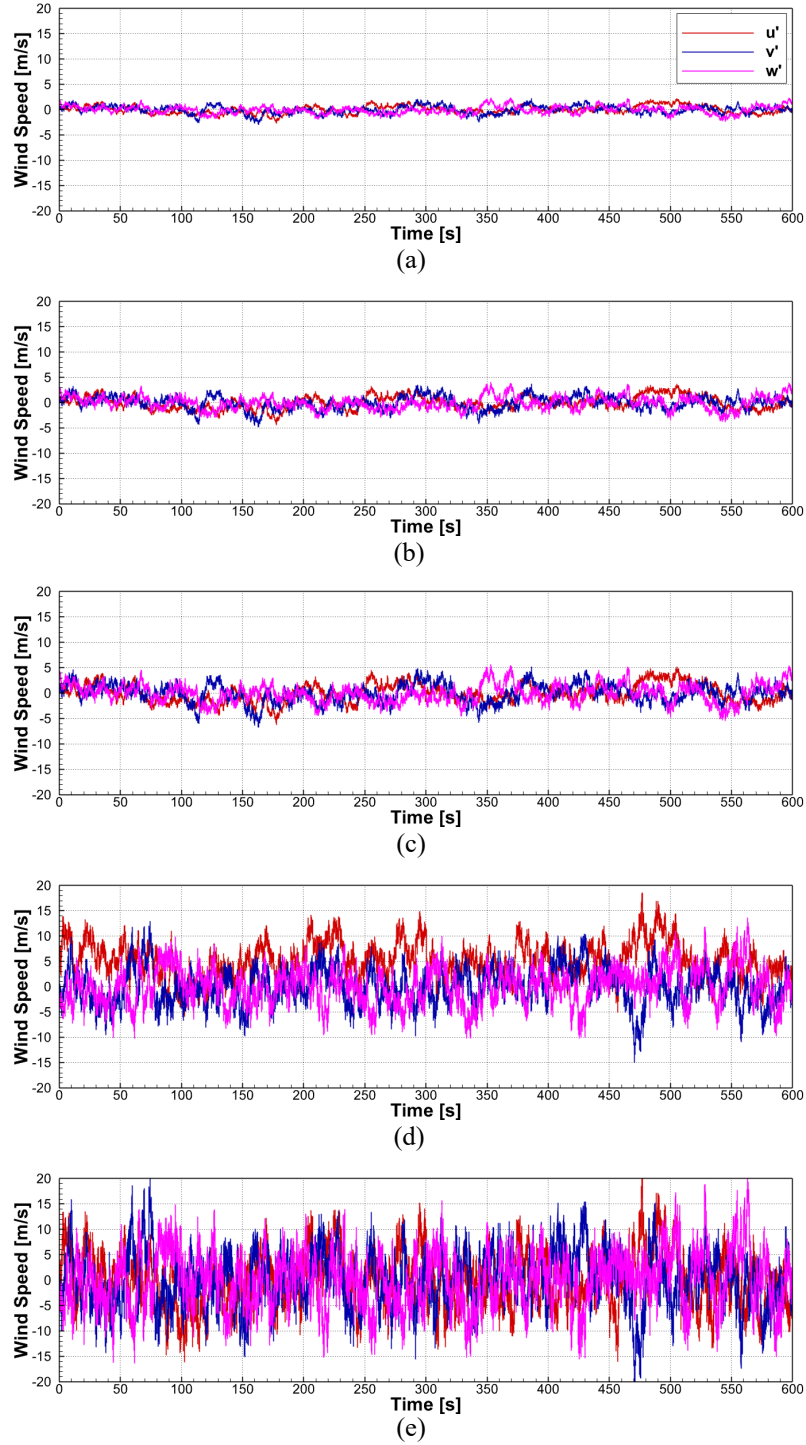


Fig. 6. Time-history curves of atmospheric disturbance components along x -, y -, and z -directions at specific points: (a) case 2: $V_{\text{wind}} = 10$ knots, $TI = 15\%$; (b) case 3: $V_{\text{wind}} = 10$ knots, $TI = 25\%$; (c) case 4: $V_{\text{wind}} = 10$ knots, $TI = 35\%$; (d) case 5: $V_{\text{wind}} = 20$ knots, $TI = 35\%$; and (e) case 6: $V_{\text{wind}} = 30$ knots, $TI = 35\%$.

The PSD of the turbulent velocity components, nondimensionalized by the square of the freestream velocity, is plotted against frequency in Fig. 7. The PSD of the turbulent velocity component in the x (longitudinal)-direction that aligned with the forward flight direction of the UAM aircraft is compared at different TI values, given that the longitudinal component (u') has higher fluctuations than the lateral (v') and vertical (w') components of the disturbance. PSD analysis is commonly employed in turbulence research to quantify the distribution of energy across different frequencies, providing insights into the scale and strength of vortical structures within flow. All three cases share the same TI value (35%) but differed in V_{wind} value. The case with the highest V_{wind} (30 knots) exhibits the highest overall spectral energy, indicating stronger and more energetic turbulence fluctuations. Furthermore, an increase in V_{wind} value leads to a shift in the cutoff frequency of the turbulent velocity, with higher-speed cases having higher-frequency content. This is attributed to the faster advection of small-scale eddies, resulting in a broader frequency range of disturbance input to the rotor system. Such shifts in turbulence spectra are critical for analyzing how inflow disturbances couple with rotor dynamics and affect unsteady aerodynamic loads and noise generation.

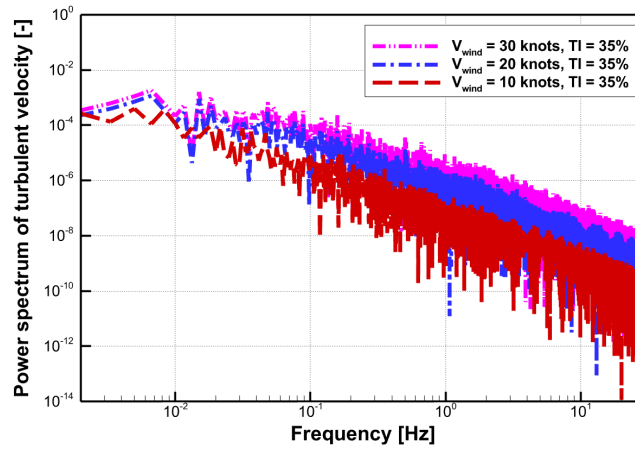


Fig. 7. Nondimensionalized power spectrum density of turbulent velocity along the x -direction at a specific point.

4. Results and Discussion

Six simulation cases are explored to assess the influence of atmospheric turbulence on the aerodynamic and aeroacoustic performance of a full-configuration SbS UAM aircraft, as detailed in Table 4. All case studies have the same forward flight velocity, rotational speed, and pilot input. The cases are systematically constructed by varying the V_{wind} and TI values, reflecting a progressive increase in turbulence severity. The first part of this section is devoted to studying the impact of atmospheric turbulent inflow on the aerodynamic performance of a cruising SbS UAM aircraft at $\mu = 0.15$. In the second part, the aeroacoustic characteristics of a cruising SbS UAM aircraft at $\mu = 0.15$ are investigated. A consistent contour legend is employed in all cases to facilitate comparisons of the findings.

4.1 Turbulence inflow effects on UAM aerodynamics

The SbS rotor system, like other twin main rotor systems with contra-rotating rotors of equal size, such as tandem and coaxial systems, have improved aerodynamic performance and stability at high forward speeds compared to conventional single rotor systems, enabling them to carry larger payloads. However, their wake structure is more complicated. In forward flight, the wake generated by SbS rotors plays a critical role in determining the unsteady aerodynamic and aeroacoustic characteristics of UAM aircraft. The rotor tip vortices and wake structures convect downstream, interacting with the fuselage, adjacent rotors, or their own blades, inducing complex flow phenomena such as unsteady loading, aerodynamic interference, and BVI. These interactions are known to cause aerodynamic instability and impulsive noise, particularly during forward and descending flight maneuvers. Accurate prediction of rotor wake is essential for reliable analysis of rotor performance, structural load, vibration, and noise in multirotor configurations.

Fig. 8 depicts the wake field structure of the SbS rotor system during cruising operations. Tip vortices, with a large vorticity magnitude, play a critical role in inducing load on aircraft [63]. Tip vortex spirals (also called blade tip vortex rings) push backward during forward flight, inducing downwash velocity in the opposite thrust direction. Similar to the wing tip vortices in finite fixed-wing aircraft, rotorcraft blade tip vortices form interlocking swirling flows, creating strong counterclockwise and clockwise rolled-up tip vortices, also known as super vortices [75].

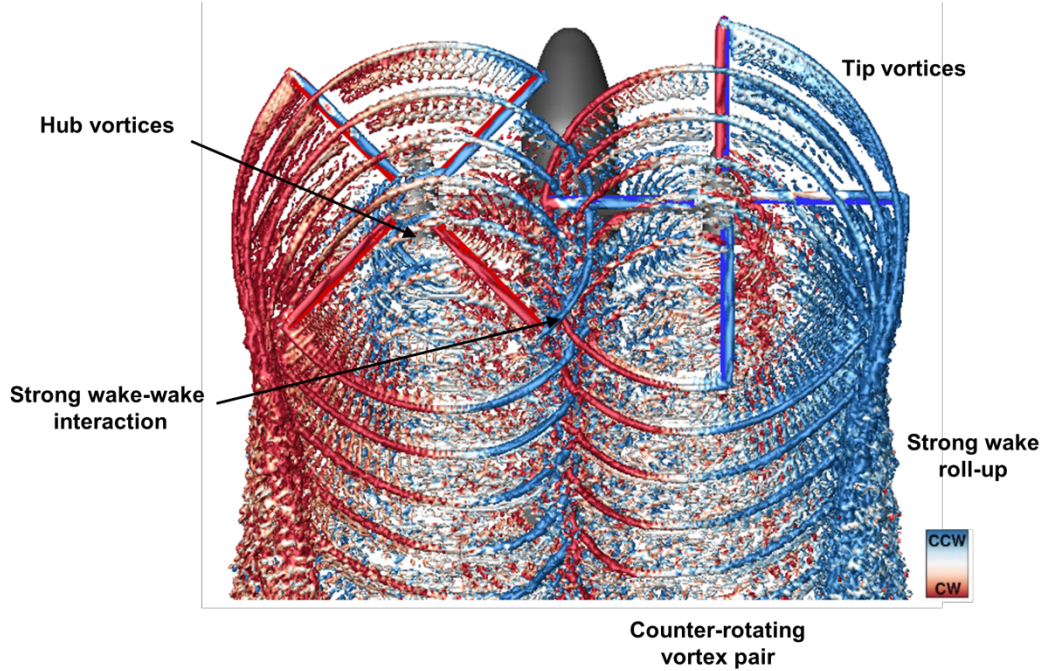


Fig. 8. Wake structure of SbS rotor under forward flight conditions. CCW, counterclockwise; CW, clockwise.

The rolled-up tip vortices at the exterior of the rotor system (advancing side of each rotor) produce a strong downwash in the region between them, thus creating a strong upwash outside of this region. The pair of super vortices, which are rolled up from the tip vortices, drag weak hub vortices into their swirls. Within the overlapping area (retreating side of each rotor), the tip vortices of each rotor interact with the rolled-up tip vortices generated by the other rotor, resulting in a strong interlocking wake structure. The isosurface of the Q-criterion field, colored by the wake swirl magnitude in Fig. 8, is defined as follows [87]:

$$\text{swirl} = \frac{\boldsymbol{\omega} \cdot \mathbf{V}_{\text{mean}}}{\rho \|\mathbf{V}_{\text{mean}}\|^2} \quad (19)$$

where $\boldsymbol{\omega}$ is the vorticity and ρ is the density. The CCW and CW directions (from behind the aircraft) of the super vortices at the advancing side of the rotors are well illustrated in Fig. 8. The merged tip vortices at the retreating side of the rotors in the overlapped region induce a substantial downwash in the overlapped area. Interaction between the wakes generated by the rotors and their impingement with the fuselage and blades result in strong unsteadiness in aerodynamic loads.

Figs. 9 and 10 compare variations in the integrated thrust coefficient of the SbS rotor blades during the last four revolutions under the impacts of TI (cases 1–4) and wind speed (cases 1 and 4–6). Collision of the strong tip vortices shed from one blade with respect to the preceding blade causes a sudden change in the effective angle of attack of the rotor blade, leading to impulsive loading. Sudden load changes could also stem from BVI events occurring within a shorter period (i.e., higher frequency). Impulsive loading of the SbS rotor system is evident in case 1, without atmospheric turbulence. Given that the mean forward flight speed is the same for all cases, the average thrust values are also consistent. However, given that the turbulence severity of the atmospheric inflow increases with increasing TI or V_{wind} value, the amplitude and frequency of the loading variations also increase. Furthermore, in uniform wind flow, the aerodynamic loads exhibit steady changes once the rotorcraft wake reaches a stable state. By contrast, the time-history curves of the aerodynamic loads in turbulent atmospheric inflow display strong instabilities in amplitude and frequency. A comparison of Figs. 9 and 10 indicates that both the amplitude and frequency of load fluctuations increase with wind velocity. To quantify the time-variation of aerodynamic loads, the root mean square (RMS) deviation of the thrust coefficient is defined as:

$$\text{RMS} = \sqrt{\frac{1}{N} (C_T - C_{T,\text{mean}})^2} \quad (20)$$

The RMS values for all test cases are summarized in Table 5, highlighting the influence of mean wind velocity and turbulence intensity on aerodynamic load fluctuation. The results indicate a progressive increase in RMS with higher turbulence severity and wind speed, from 1.72×10^{-4} for the uniform inflow case (Case 1) to 9.69×10^{-4} for the most severe turbulence condition (Case 6). This trend reflects the greater wake unsteadiness and aerodynamic load variability induced by stronger turbulence, which can elevate noise levels and potentially increase the structural vulnerability of UAM aircraft. Therefore, the influence of such load fluctuations should be carefully considered in the aerodynamic and structural design stages.

Table 5. Root mean square (RMS) deviation of the thrust coefficient for all test cases,

Case	Mean wind velocity [knot]	Turbulence intensity (TI) [%]	RMS ($\times 10^{-2}$)
1	0	0	0.0172
2	10	15	0.0182
3	10	25	0.0243

4	10	35	0.0315
5	20	35	0.0613
6	30	35	0.0969

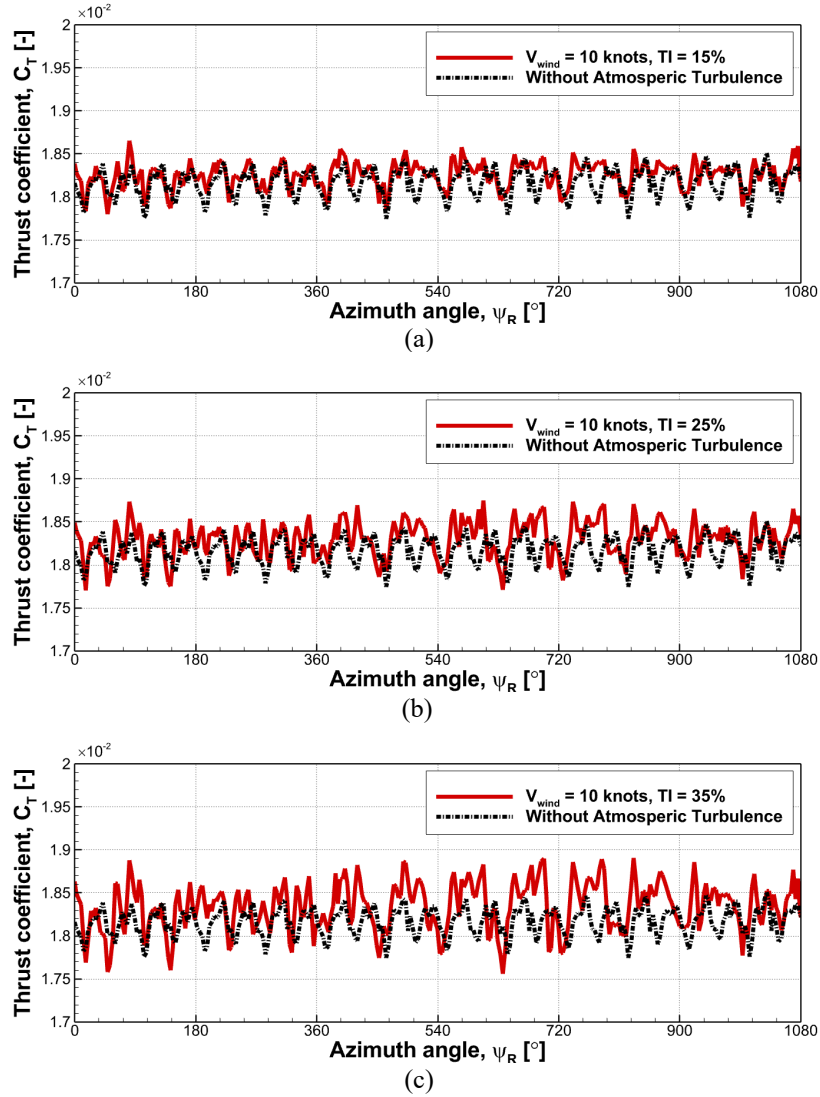


Fig. 9. Comparison of time-history curves of the thrust coefficient (C_T) of SbS UAM aircraft at different turbulence intensity (TI) values and constant mean wind velocity. (a) Case 2: $V_{wind} = 10$ knots, $TI = 15\%$, (b) case 3: $V_{wind} = 10$ knots, $TI = 25\%$, and (c) case 4: $V_{wind} = 10$ knots, $TI = 35\%$.

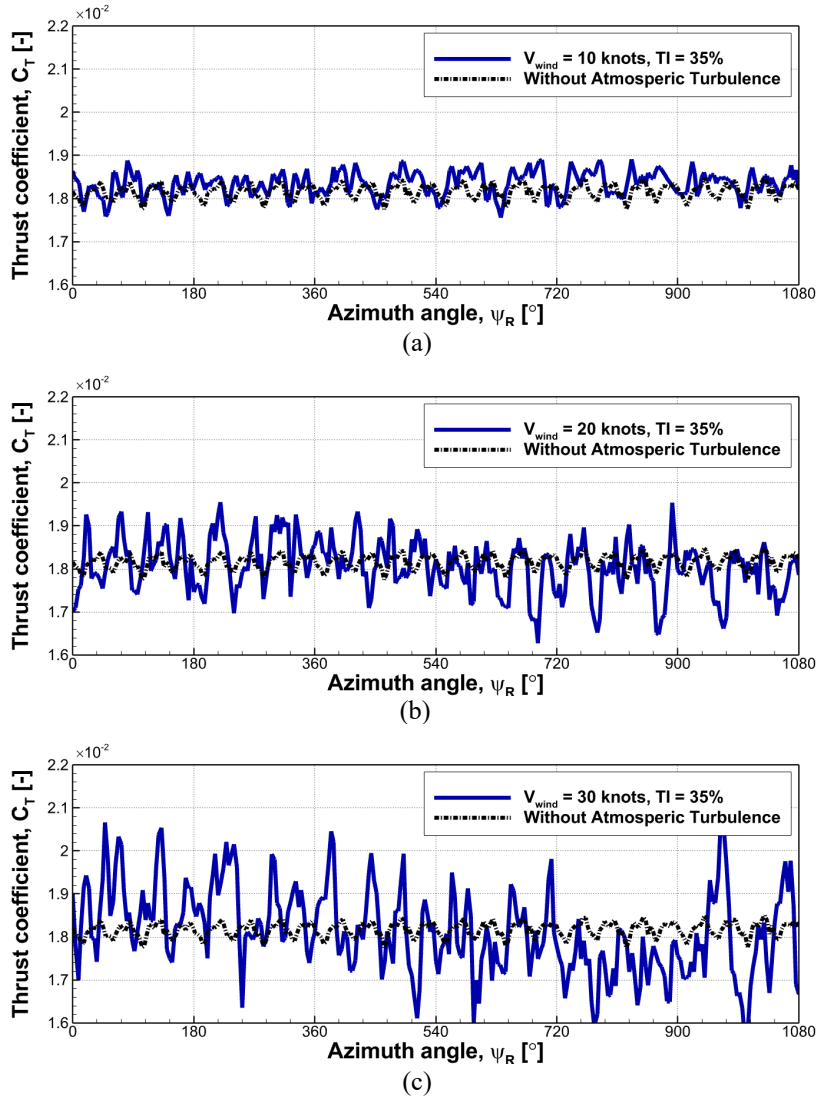
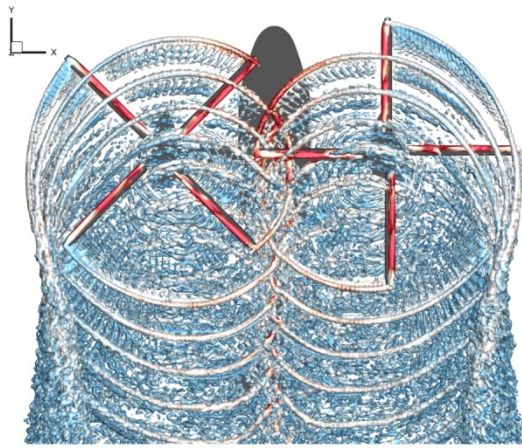


Fig. 10. Comparison of time-history curves of the thrust coefficient (C_T) of SbS UAM aircraft at different mean wind velocity (V_{wind}) values and constant turbulence intensity (TI). (a) Case 4: $V_{wind} = 10$ knots, $TI = 35\%$, (b) case 5: $V_{wind} = 20$ knots, $TI = 35\%$, and (c) case 6: $V_{wind} = 30$ knots, $TI = 35\%$.

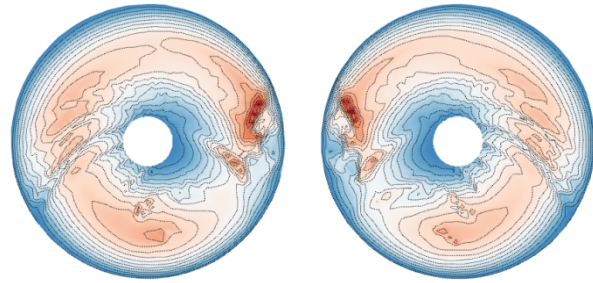
Although tip vortices cause the most pronounced load changes, collision of the shedding and trailing vortices that depart from the trailing edge of the rotor blade with other blades, known as blade–wake interactions, also influence aerodynamic performance (Fig. 8). The mechanism underlying the aerodynamic load fluctuations of the rotor system can be sought in the wake structures generated by the full-configuration SbS UAM aircraft at varying turbulence characteristics and $\mu = 0.15$, as depicted in Fig. 11. In this figure, the isosurface of the Q-criterion field [87], colored by the vorticity magnitude, illustrates the wake field, demonstrating super vortices swirling behind the

rotorcraft and the shedding vortex rings. All cases have the same Q-criterion values and vorticity magnitude contour range. The mixing tip vortices in the overlapping region of the rotorcraft are easily observed in Fig. 8, and rotor-wake interaction and BVI, which cause load fluctuations, are evident. Collision of tip vortices occurs in the overlapping region, strengthening their impact on flow. Additionally, BVI events between the trailing vortex from one blade to another blade from the same rotor are evident in the overlapping region as well as between the vortex propagated from the blade of one rotor to the blade of the adjacent rotor (See Fig. 11(a)). Investigating the wake structure under atmospheric turbulent inflow reveals that it becomes more disturbed with increasing turbulence. Under severe turbulence conditions, the organized tip-vortex structure is significantly disrupted, reducing the probability of direct BVI events and diminishing their associated tonal noise contribution. However, the increased turbulence intensity induces larger velocity fluctuations across the rotor disk, which enhances the amplitude of unsteady aerodynamic loads on the blades. These enhanced unsteady loads increase the unsteady loading noise predicted by the FW-H formulation. This phenomenon is attributed to blade-turbulence interaction (BTI) effects [88, 89], which become more pronounced under severe turbulence conditions. Consequently, although the contribution from BVI noise decreases, the increase in unsteady loading noise due to BTI effects can outweigh this reduction, leading to an overall rise in the total noise level.

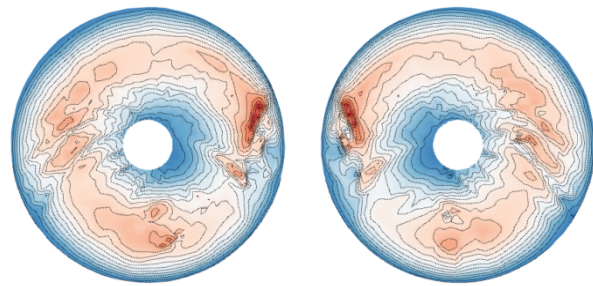
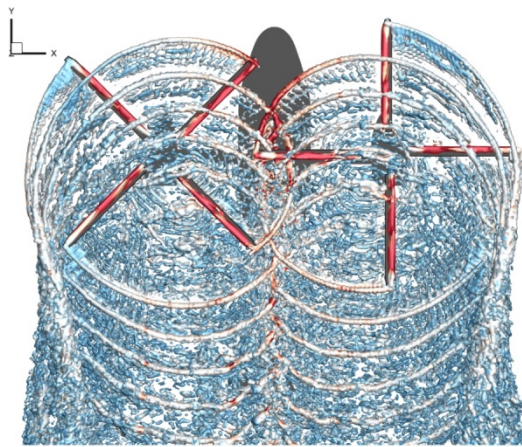
The influence of this wake distortion is manifested by the azimuthal distribution of the sectional thrust coefficient on the rotor plane, as shown in the right column of Fig. 11. Rapid variation in load distribution in the overlapping region between rotors occurs with substantial impulsive load changes at the entrance ($\psi = 150^\circ$) and exit ($\psi = 212^\circ$) of the overlapping area for both rotors, indicating the occurrence of BVI from the opposite rotor. In the downwind direction of the rotors, the blade is affected by tip vortex rings and trailed hub vortices, causing loading variations. Considering the rotational direction of the emanated tip vortices and that the induced velocity generated from one vortex tube causes an upward velocity on one side of the vortex tube and downwash velocity on the other [90], helps to understand the variation in thrust load on the rotor disc. Comparing Fig. 11(a) with Fig. 11(f) shows that as the severity of the turbulence inflow increases, the blade-turbulence interactions effects become dominant, causing reduction in wake coherence and azimuthal variation in rotor-disk loading. As a result, the time histories of the aerodynamic load exhibit larger fluctuation amplitudes, reflecting the enhanced unsteadiness of the wake and blade loading under turbulent inflow.



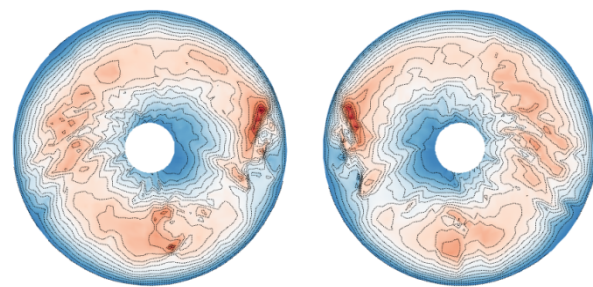
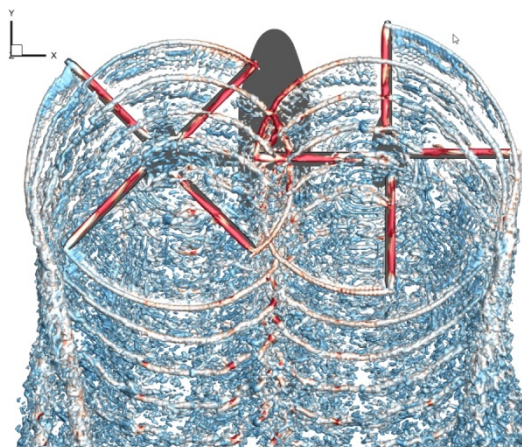
Low $M^2 C_N$ High



(a)



(b)



(c)

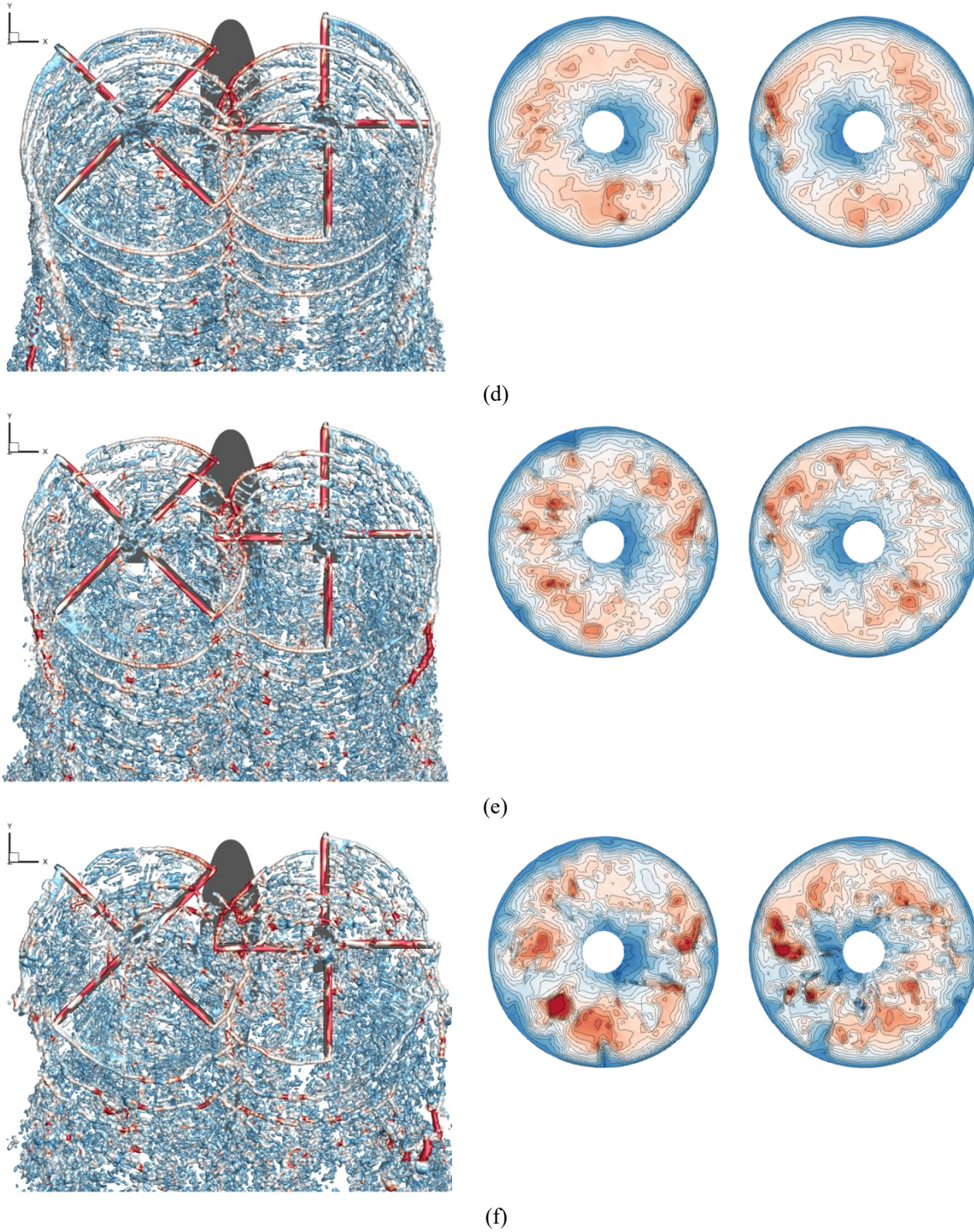
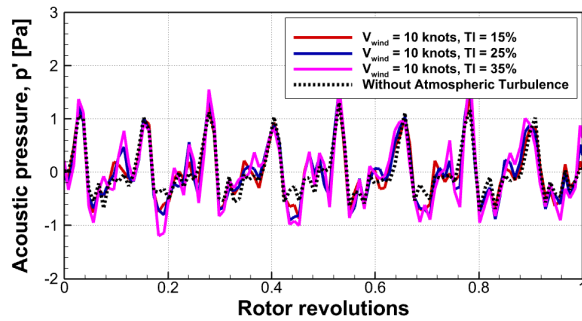


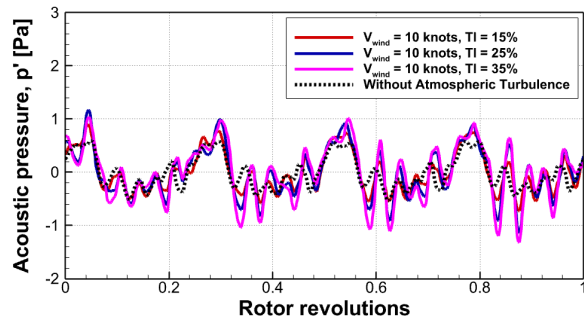
Fig. 11. Comparison of wake structure and isosurface of Q-criterion colored by vorticity magnitude (left side) and distribution of sectional normal force contour (right side) with different mean wind speed (V_{wind}) and turbulence intensity (TI) values. (a) Case 1: without atmospheric turbulence, (b) case 2: $V_{wind} = 10$ knots, $TI = 15\%$, (c) case 3: $V_{wind} = 10$ knots, $TI = 25\%$, (d) case 4: $V_{wind} = 10$ knots, $TI = 35\%$, (e) case 5: $V_{wind} = 20$ knots, $TI = 35\%$, and (f) case 6: $V_{wind} = 30$ knots, $TI = 35\%$.

4.2 Turbulence inflow effects on UAM aeroacoustics

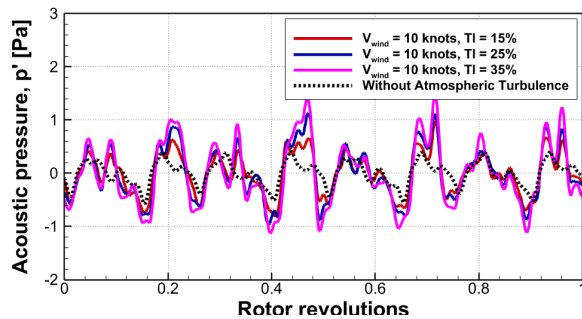
This section discusses the aeroacoustic characteristics of a cruising SbS UAM aircraft at $\mu = 0.15$ under atmospheric turbulent inflow conditions. Figs. 12 and 13 present the predictions of total acoustic pressure of the full-configuration aircraft at microphone azimuth angles (ψ_{MIC}) of 0° (aft side), 90° (starboard side), 180° (fore side), and 270° (port side) to investigate the impact of TI and wind speed on aeroacoustics, respectively. The total acoustic pressure on the rotating plane is the sum of the thickness and loading noise components. As discussed in the previous section, the unsteady nature of overlapped SbS rotor systems during cruising leads to high-frequency noise in all directions, even during operation in a clear atmosphere. The acoustic pressure levels for observers at azimuth angles of 90° and 270° are quite similar, with the slight asymmetry attributable to the phase shift and highly complex vortex flow in the inter-rotor region of overlapped rotors [74,91]. The downwind direction experiences high-loading variations owing to BVI events, and the microphone at $\psi_{MIC} = 0^\circ$ records a higher peak-to-peak sound pressure amplitude than the microphone at $\psi_{MIC} = 180^\circ$. The acoustic pressure level on the fore side ($\psi_{MIC} = 180^\circ$) is the lowest in all directions given that the rotor wake propagates in the downwind, where the most pronounced interactions occur.



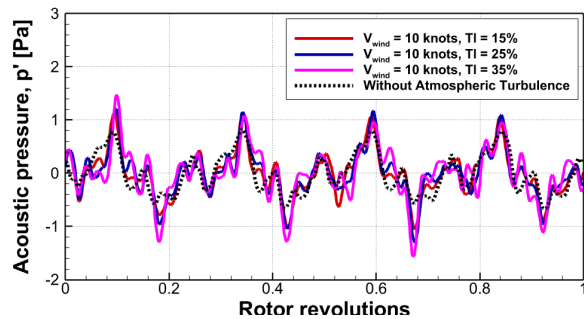
(a)



(b)



(c)



(d)

Fig. 12. Comparison of overall acoustic pressure for cases 1–4 at different turbulence intensity (TI) values: (a) observer at $\Psi_{MIC} = 0^\circ$, (b) observer at $\Psi_{MIC} = 90^\circ$, (c) observer at $\Psi_{MIC} = 180^\circ$, and (d) observer at $\Psi_{MIC} = 270^\circ$.

As shown in Figs. 12 and 13, the recorded peaks in total acoustic pressure increase in all directions with increasing TI value. The pattern of acoustic pressure variation on the aft side of the UAM aircraft does not substantially change, which was expected given that the dominant wake structures are maintained on the aft side of the aircraft for cases 2–4 in Fig. 11. However, this is not the case in other directions, especially for case 4, where the pattern of acoustic pressure variation changes slightly (Fig. 11(d)). The acoustic pressure levels presented in Fig. 12 reveal that the noise characteristics of the SbS AUM aircraft are greater in the downwind direction ($\Psi_{MIC} = 0^\circ$) than in other directions. Figs. 11(e, f) demonstrates that the aircraft can no longer maintain its dominant organized wake structure with increasing severity of turbulent inflow (i.e., increasing wind speed), which impacts the loading distribution pattern. Accordingly, the pattern of acoustic pressure variation changes in all directions, particularly for case 6, as shown in Fig. 13. Additionally, the aircraft does not exhibit a dominant noise side.

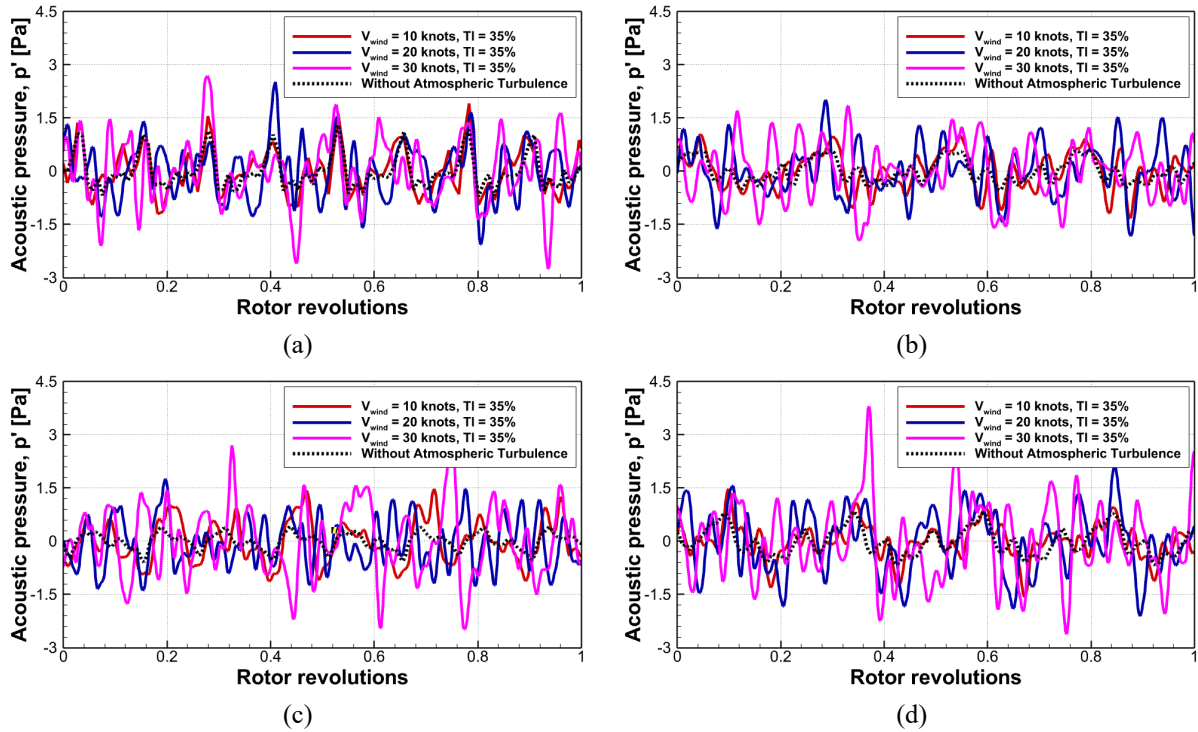


Fig. 13. Comparison of overall acoustic pressure for cases 1 and 4–6 at different wind speeds: (a) Observer at $\Psi_{MIC} = 0^\circ$; (b) Observer at $\Psi_{MIC} = 90^\circ$; (c) Observer at $\Psi_{MIC} = 180^\circ$; (d) Observer at $\Psi_{MIC} = 270^\circ$.

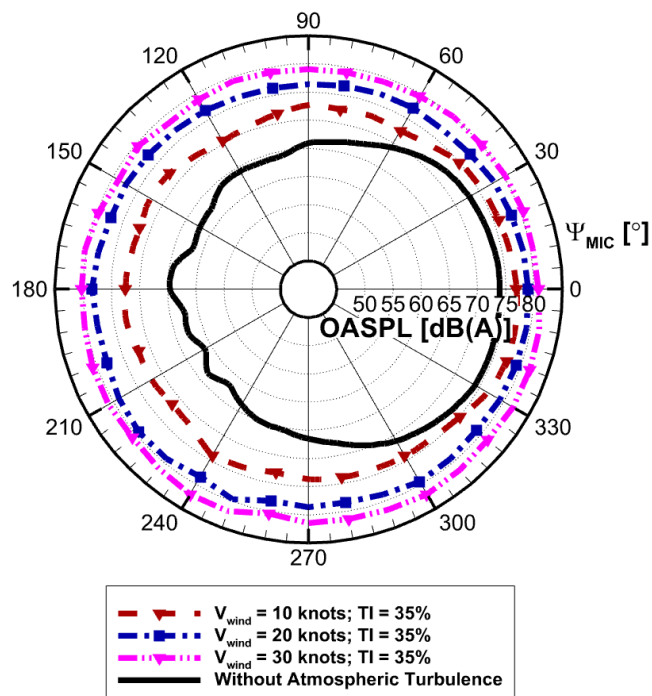
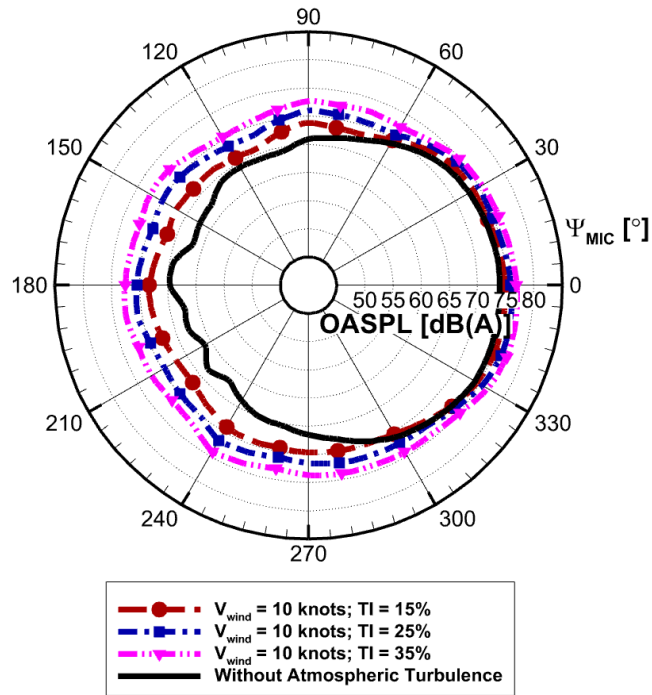


Fig. 14. A-weighted overall sound pressure levels (OASPL) of SbS UAM aircraft at various observer positions: (a) effect of turbulence intensity (TI) and (b) effect of mean wind velocity (V_{wind}).

Fig. 14 presents the A-weighted overall sound pressure level (OASPL) directivity of the SbS UAM aircraft under varying atmospheric turbulence conditions. The data are organized to examine the influence of (a) turbulence intensity (TI) at fixed mean wind velocity ($V_{\text{mean}} = 10$ knots) and (b) mean wind velocity at fixed TI (TI = 35%). In the forward flight condition, the OASPL exhibits pronounced directivity, with peak levels consistently observed in the aft side of the aircraft ($\psi_{\text{MIC}} \approx 0^\circ$) due to strong BVI phenomena. Conversely, the minimum noise levels appear in the front region of the aircraft ($\psi_{\text{MIC}} \approx 180^\circ$), which can be attributed to the high loading in the front of the overlapped area. This asymmetry aligns with the previously identified spatial distribution of acoustic sources near the advancing blades on the starboard side (see Fig. 11). In Fig. 14(a), increasing turbulence intensity results in a general rise in OASPL across all azimuthal positions. However, the rate of growth for OASPL on the fore side of the aircraft is higher than that on the aft side: on the aft side ($\psi_{\text{MIC}} = 0^\circ$), OASPL increases modestly with TI, while on the fore side ($\psi_{\text{MIC}} = 180^\circ$), the increase is more substantial. Specifically, at $\psi_{\text{MIC}} = 180^\circ$, OASPL rises from 64.63 dBA under uniform inflow to 72.55 dBA under severe turbulence, indicating a difference of nearly 7.92 dBA. In contrast, the aft-side level increases from 73.97 dBA to 76.92 dBA, yielding a smaller difference of 2.95 dBA. This disparity primarily arises from the stronger wake existing at the aft side of the aircraft compared to the fore side (see figure 11). These strong wake structures mollify the impact of turbulence wake interaction with the rotor in the aft side and thus make this side of the aircraft more resilience toward the impact of turbulence inflow. However, in the severe turbulence inflow conditions, by destruction of harmonic wake structures, the turbulence wake interaction becomes the most dominant reason in the rotor's loading fluctuations causing less localized and more randomly distributed loading fluctuation across the entire rotor disk azimuth, which results in a more uniform distribution of high sound pressure levels across different observer directions.

Fig. 14(b) demonstrates the effect of increasing mean wind velocity (V_{mean}) at constant turbulence intensity (TI = 35%). As the inflow velocity increases from 10 to 30 knots, the OASPL rises across the entire azimuthal range, with more pronounced amplification on the fore side. The results indicate that the difference in the measured OASPLs for a SbS UAM aircraft cruising through the most severe atmospheric turbulent inflow (case 6: $V_{\text{mean}} = 30$ knots and TI = 35%) compared to a clear atmosphere (case 1) is approximately 7 dBA at $\psi_{\text{MIC}} = 0^\circ$, whereas this difference is nearly 16 dBA at $\psi_{\text{MIC}} = 180^\circ$. This variation can be attributed to both enhanced aerodynamic loading

and increased turbulence kinetic energy in the inflow field. The directivity patterns shown in Fig. 14(a) and Fig. 14(b) highlights that both TI and V_{mean} influence directly noise propagation mechanisms, particularly through their interaction with rotor wake dynamics and the downstream evolution of flow structures. Overall, these findings indicate the substantial influence of atmospheric turbulence on the acoustic characteristics of UAM vehicles, demonstrating that turbulence not only increases overall noise levels but also alters directivity patterns.

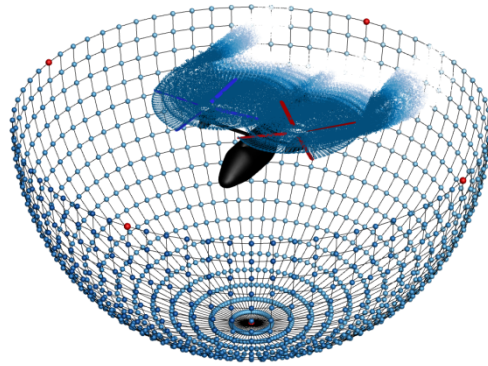
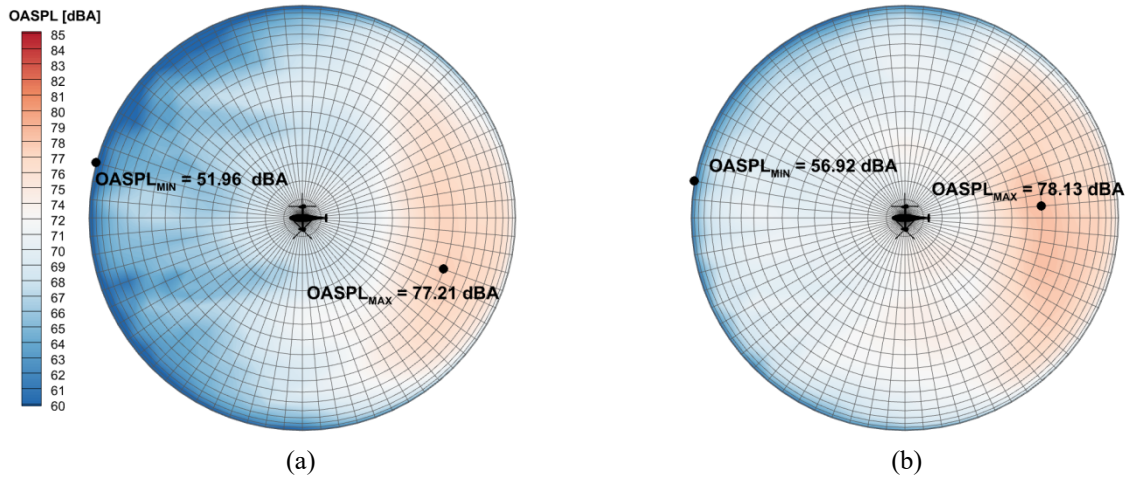


Fig. 15. Hemisphere arrangement of microphones below the SbS UAM aircraft with a radius of 50 m from the center of the rotors (not drawn to scale).



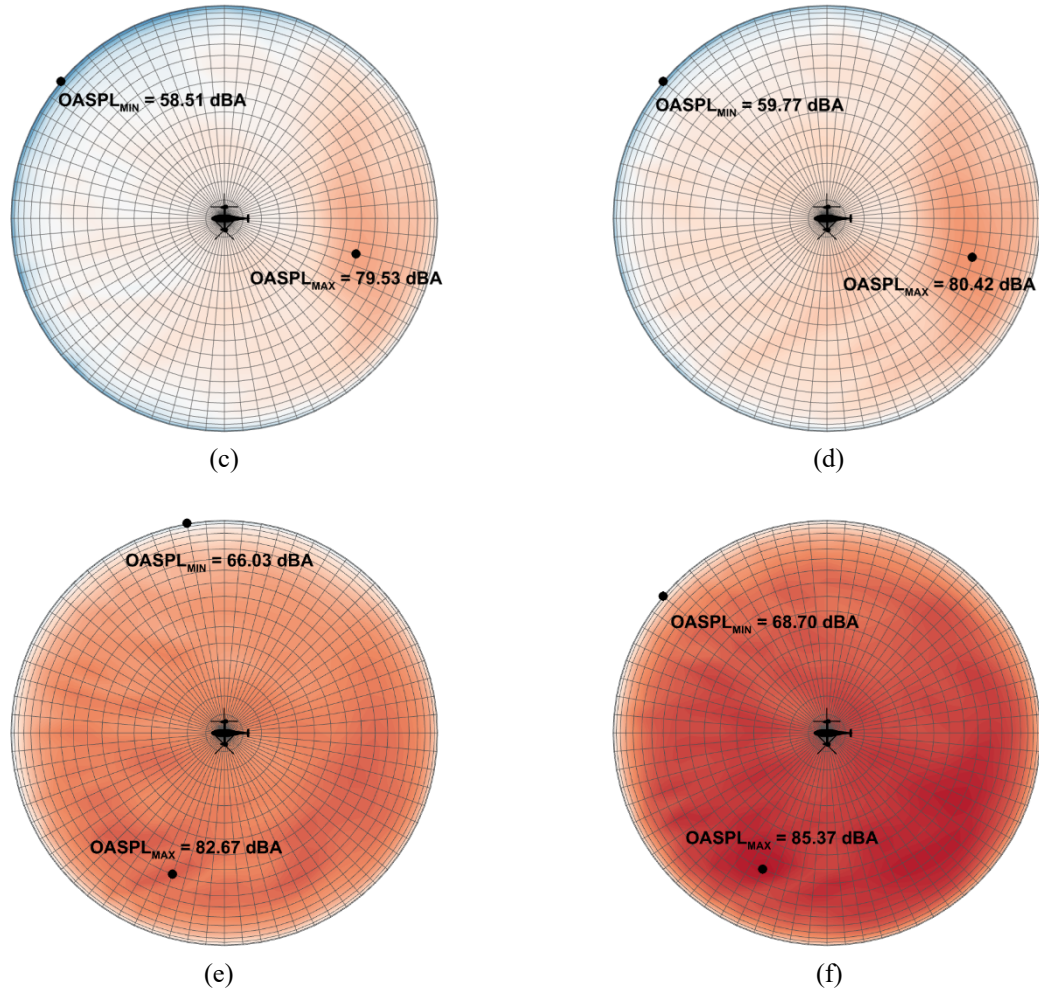


Fig. 16. Three-dimensional representation of OASPL evaluated on the hemisphere below the rotor system (top view): (a) case 1: without atmospheric turbulence, (b) case 2: mean wind speed = 10 knots, TI = 15%, (c) case 3: mean wind speed = 10 knots, TI = 25%, (d) case 4: mean wind speed = 10 knots, TI = 35%, (e) case 5: mean wind speed = 20 knots, TI = 35%, and (f) case 6: mean wind speed = 30 knots, TI = 35%.

To further investigate the influence of atmospheric turbulent inflow on the aeroacoustic behavior of SbS UAM aircraft during forward flight ($\mu = 0.15$), a hemispherical microphone array was employed, as illustrated in Fig. 15. The hemisphere, centered 50 m below the rotor hub and with a radius of 50 m ($\approx 16R$), was discretized at 5° intervals in both azimuthal (ψ) and elevation (ϕ) directions. This configuration enables a detailed three-dimensional assessment of the radiated noise field surrounding the aircraft. Fig. 16 presents the spatial distribution of A-weighted OASPL evaluated onto the hemispherical surface for all six turbulence cases. In the baseline condition without atmospheric turbulence (case 1), the noise directivity exhibits a clear asymmetry, with significantly higher OASPL

observed in the aft quadrant compared to the fore region. This result is consistent with the intense BVI events occurring downstream of the aircraft, particularly concentrated within the angular sectors of $-35^\circ < \psi_{\text{MIC}} < 15^\circ$ and $30^\circ < \phi_{\text{MIC}} < 55^\circ$. These high-noise regions align with the strong wake impingement and unsteady loading effects induced by the rotor–wake interactions. This pattern is observed for cases 1–4 but not for cases 5 and 6, where the aircraft is under the most severe turbulent inflows. As the turbulence intensity increases, the OASPL distribution becomes more uniformly elevated across the hemisphere, indicating that atmospheric turbulent inflow not only amplifies the overall noise levels but also broadens the region with high OASPLs. In particular, for cases 5 and 6, representing the most severe turbulent inflow conditions, nearly the entire hemisphere exhibits elevated noise levels, indicating that atmospheric turbulence disrupts the coherent wake structures and increases acoustic energy over a wider range of observer positions. Quantitatively, the maximum OASPL values across cases 1 to 6 are 77.21, 78.13, 79.53, 80.43, 82.67, and 85.37 dBA, while the minimum values are 51.96, 56.92, 58.51, 59.77, 66.03, and 68.70 dBA, respectively. These results confirm that both the noise levels increase monotonically with turbulence intensity. The amplification in minimum OASPL also indicates a significant reduction in noise directivity, implying that turbulent inflow conditions can lead to more omnidirectional noise radiation characteristics in UAM operations.

5. Conclusion

This study employs an efficient, mid-fidelity, coupled nonlinear vortex method integrated with the FW–H acoustic analogy and a stochastic full-field inflow turbulence generator to investigate the aerodynamics and aeroacoustics of NASA’s full-configuration SbS UAM aircraft while cruising through atmospheric turbulent inflow. Six atmospheric turbulence levels are selected to evaluate the impact of turbulence severity on aircraft performance. The wake structure of the cruising SbS rotor system comprises four main components: a pair of strong rolled-up tip vortices on the advancing side of each rotor, complex interlocked roll-up tip vortices on the retreating side, an overlapping region, and tip vortex spirals (blade tip vortex rings). These wake structures play critical roles in the unsteadiness and impulsive loading of the SbS rotor system. Under uniform wind conditions, aerodynamic loads exhibit steady variations once the rotor wake reaches a converged state. However, the organized wake structures become increasingly disrupted and eventually deteriorate with increasing turbulence severity.

The simulation results show that the BTI phenomena and harmonic BVI play the dominant role in determining the aerodynamic and aeroacoustic performance of the SbS UAM aircraft under atmospheric turbulence inflow condition. As the severity of the turbulence inflow increases, the impact of BTI becomes more dominant compared to BVI event. Higher turbulence severity results in elevated SPLs and altered aeroacoustic patterns. The impact of turbulent inflow on noise emission is less pronounced on the aft region of the aircraft compared to other directions. This difference is attributed to the dominant wake structure propagating downward, which mitigates the influence of atmospheric turbulence in that region. The noise hemisphere beneath the aircraft revealed that, in a clear atmosphere, the high OASPL region is concentrated in the aft quadrant and inclined to the overlapping wake region, where intensive harmonic BVI events occur behind the aircraft. However, the high SPL region expands with intensifying turbulent inflow. Notably, nearly the entire hemisphere beneath the aircraft experienced high OASPLs in the most severe turbulence scenario.

Accurate performance assessments under realistic atmospheric turbulent inflow are crucial during the preliminary design stages of UAM aircraft. The model introduced in this study provides valuable insights into the flow physics, unsteady wake behavior, and noise characteristics of SbS UAM aircraft and other multirotor UAM configurations during cruising operations in urban atmospheric turbulence. This information can support the development of advanced designs and operational guidelines, thereby enhancing the robustness, safety, and acoustic comfort of UAM aircraft. The present numerical model provides a computationally efficient framework for simulating the aerodynamic and aeroacoustic performance of a full-configuration UAM aircraft under atmospheric turbulent inflow. However, several limitations should be acknowledged. The present framework based on potential flow is not capable of fully capturing the influence of spatially distributed turbulence inflow and dissipation near solid surfaces, and the synthetic turbulence generated by TurbSim does not include wall-bounded interactions with the blade or fuselage. In addition, the viscous diffusion of vorticity is not explicitly modeled in the VPM, which could affect the accuracy of long-term far-wake predictions, and the acoustic analysis focuses solely on loading and thickness noise, excluding airfoil self-noise such as TE and TI noise. Future work will address these limitations by incorporating wall-resolved turbulence modeling, implementing viscous diffusion effects through the particle strength exchange (PSE) method, and extending the acoustic framework to include TE and TI noise, enabling a more comprehensive evaluation of UAM rotor performance in realistic operating environments.

Declaration of competing for interest

The authors declare that they have no known competing financial interests or personal relationships that could have appeared to influence the work reported in this paper.

Acknowledgments

This study was supported by the National Research Foundation of Korea (NRF) grant funded by the Ministry of Science and ICT (Project Number: RS-2024-00397400). This research was supported by ‘regional innovation megaproject’ program through the Korea Innovation Foundation funded by Ministry of Science and ICT (Project Number: RS-2023-IN231026). This work was supported by the Glocal University 30 Project Fund of Gyeongsang National University in 2025.

References

- [1] P. Pradeep, and P. Wei, “Energy efficient arrival with RTA constraint for urban eVTOL operations,” in Proceedings of the 2018 AIAA Aerospace Sciences Meeting, Kissimmee, FL. American Institute of Aeronautics and Astronautics; Reston, Virginia, 2018.
- [2] A. Bauranov, and J. Rakas, “Designing airspace for urban air mobility: A review of concepts and approaches,” Prog. Aerosp. Sci. 125, 100726 (2021). DOI: [10.1016/j.paerosci.2021.100726](https://doi.org/10.1016/j.paerosci.2021.100726).
- [3] P. Fontaine, Urban air mobility (UAM) concept of operations V2, U.S. Department of Transportation, Washington, DC, 2023. https://www.faa.gov/air-taxis/uam_blueprint.
- [4] M.H. Masum, S.K. Pal, A.A. Akhie, I.J. Ruva, N. Akter, and S. Nath, “Spatiotemporal monitoring and assessment of noise pollution in an urban setting,” Environ. Chall. 5, 100218 (2021). DOI: [10.1016/j.envc.2021.100218](https://doi.org/10.1016/j.envc.2021.100218).
- [5] J. Ma, C. Li, M.-P. Kwan, L. Kou, and Y. Chai, “Assessing personal noise exposure and its relationship with mental health in Beijing based on individuals’ space-time behavior,” Environ. Int. 139, 105737 (2020). DOI: [10.1016/j.envint.2020.105737](https://doi.org/10.1016/j.envint.2020.105737).

- [6] S. Li, and S. Lee, “Prediction of urban air mobility multirotor VTOL broadband noise using UCD-QuietFly,” *J. Am. Helicopter Soc.* 66(3), 1–13 (2021). DOI: [10.4050/JAHS.66.032004](https://doi.org/10.4050/JAHS.66.032004).
- [7] Z.H. Jia, and S. Lee, “Computational study on noise of urban air mobility quadrotor aircraft,” *J. Am. Helicopter Soc.* 67(1), 1–15 (2022). DOI: [10.4050/JAHS.67.012009](https://doi.org/10.4050/JAHS.67.012009).
- [8] J. Kim, “Urban air mobility noise: Further considerations on indoor space,” *Int. J. Environ. Res. Public Health* 19(18), 11298 (2022). DOI: [10.3390/ijerph191811298](https://doi.org/10.3390/ijerph191811298).
- [9] H. Eißfeldt, “Sustainable urban air mobility supported with participatory noise sensing,” *Sustainability* 12(8) (2020). DOI: [10.3390/su12083320](https://doi.org/10.3390/su12083320).
- [10] Z. Jia, and S. Lee, “High-fidelity computational analysis on the noise of a side-by-side hybrid VTOL aircraft,” *J. Am. Helicopter Soc.* 67(2), 1–14 (2022). DOI: [10.4050/JAHS.67.022005](https://doi.org/10.4050/JAHS.67.022005).
- [11] J. Sagaga, and S. Lee, “Performance, aerodynamics, and aeroacoustics of side-by-side rotors using high-fidelity computational fluid dynamics,” *AIAA J.* 61(12), 5429–5445 (2023). DOI: [10.2514/1.J062955](https://doi.org/10.2514/1.J062955).
- [12] J. Sagaga, and S. Lee, “High-fidelity computational study of aerodynamic noise of side-by-side rotor in full configuration,” *J. Sound Vib.* 592, 118607 (2024). DOI: [10.1016/j.jsv.2024.118607](https://doi.org/10.1016/j.jsv.2024.118607).
- [13] K.S. Brentner, G.A. Bres, G. Perez, and H.E. Jones, “Maneuvering rotorcraft noise prediction: A new code for a new problem,” in *AHS Aerodynamics, Acoustics and Test Evaluation Specialist Meeting*. San Francisco, CA, 2002.
- [14] K.S. Brentner, and F. Farassat, “Modeling aerodynamically generated sound of helicopter rotors,” *Prog. Aerosp. Sci.* 39(2–3), 83–120 (2003). DOI: [10.1016/S0376-0421\(02\)00068-4](https://doi.org/10.1016/S0376-0421(02)00068-4).
- [15] P. Ventura Diaz, and S. Yoon, “Computational study of NASA’s quadrotor urban air taxi concept,” in *AIAA Scitech 2020 Forum*, American Institute of Aeronautics and Astronautics; Reston, Virginia, 2020. DOI: [10.2514/6.2020-0302](https://doi.org/10.2514/6.2020-0302).
- [16] V. Ahuja, D.S. Little, J. Majdalani, and R.J. Hartfield, “On the prediction of noise generated by urban air mobility (UAM) vehicles. II. Implementation of the Farassat F1A formulation into a modern surface-vorticity panel solver,” *Phys. Fluids* 34(11), 116118 (2022). DOI: [10.1063/5.0105002](https://doi.org/10.1063/5.0105002).
- [17] D.S. Little, J. Majdalani, R.J. Hartfield, and V. Ahuja, “On the prediction of noise generated by urban air mobility (UAM) vehicles. I. Integration of fundamental acoustic metrics,” *Phys. Fluids* 34(11), 116117 (2022). DOI: [10.1063/5.0105002](https://doi.org/10.1063/5.0105002).

- [18] S. Cantos, P. Zhou, H. Wu, Z. Ma, W. Chen, S. Zhong, and X. Zhang, “Aerodynamics and aeroacoustics of ducted propellers: A study on the design and geometry effects,” *Phys. Fluids* 36(3), 35116 (2024). DOI: [10.1063/5.0191323](https://doi.org/10.1063/5.0191323).
- [19] H. Wu, W. Chen, H. Jiang, S. Zhong, and X. Zhang, “Experimental investigation of the effect of sectional airfoil profile deviation on propeller noise,” *Phys. Fluids* 35(2), 27104 (2023). DOI: [10.1063/5.0135555](https://doi.org/10.1063/5.0135555).
- [20] R. Wang, Z. Ma, and X. Huang, “Experimental investigation of ducted fan noise control by turbulence grids insertion between propellers and struts,” *Phys. Fluids* 36(8), 85109 (2024). DOI: [10.1063/5.0213094](https://doi.org/10.1063/5.0213094).
- [21] S.J. Kim, Y.-H. Hwang, R.S. Myong, and H. Lee, “Interactional aerodynamics and acoustics of a rotor with an airframe in hover,” *Phys. Fluids* 36(1), 17121 (2024). DOI: [10.1063/5.0185036](https://doi.org/10.1063/5.0185036).
- [22] H. Lee, and D.-J. Lee, “Rotor interactional effects on aerodynamic and noise characteristics of a small multirotor unmanned aerial vehicle,” *Phys. Fluids* 32(4), 47107 (2020). DOI: [10.1063/5.0003992](https://doi.org/10.1063/5.0003992).
- [23] K. Yu, J. Ko, Y. Kim, and S. Lee, “Comparison of aerodynamic and aeroacoustic characteristics of fixed-pitch and variable-pitch rotors,” *Phys. Fluids* 36(9), 97169 (2024). DOI: [10.1063/5.0230264](https://doi.org/10.1063/5.0230264).
- [24] Y.-T. Wu, and F. Porté-Agel, “Atmospheric turbulence effects on wind-turbine wakes: An LES study,” *Energies* 5(12), 5340–5362 (2012). DOI: [10.3390/en5125340](https://doi.org/10.3390/en5125340).
- [25] R. Krishnamurthy, R.K. Newsom, L.K. Berg, H. Xiao, P.-L. Ma, and D.D. Turner, “On the estimation of boundary layer heights: A machine learning approach,” *Atmos. Meas. Tech.* 14(6), 4403–4424 (2021). DOI: [10.5194/amt-14-4403-2021](https://doi.org/10.5194/amt-14-4403-2021).
- [26] N. Carpman, Turbulence intensity in complex environments and its influence on small wind turbines, Department of Earth Sciences, Uppsala University, Uppsala, 2011. <http://uu.diva-portal.org/smash/get/diva2:415655/FULLTEXT01.pdf>.
- [27] B.A. Hamilton, Urban air mobility (UAM) market study: Final report, National Aeronautics and Space Administration (NASA), Washington, DC, 2018. <https://ntrs.nasa.gov/citations/20190001472>.
- [28] N.S. Jamaluddin, A. Celik, K. Baskaran, D. Rezgui, and M. Azarpeyvand, “Experimental analysis of a propeller noise in turbulent flow,” *Phys. Fluids* 35(7), 75106 (2023). DOI: [10.1063/5.0153326](https://doi.org/10.1063/5.0153326).
- [29] S.T. Go, M.J. Kingan, L. Bowen, and M. Azarpeyvand, “Noise of a shrouded propeller due to ingestion of grid-generated turbulence,” *J. Sound Vib.* 571, 118044 (2024). DOI: [10.1016/j.jsv.2023.118044](https://doi.org/10.1016/j.jsv.2023.118044).

- [30] P.J. Richards, R.P. Hoxey, B.D. Connell, and D.P. Lander, “Wind-tunnel modelling of the Silsoe Cube,” *J. Wind Eng. Ind. Aerodyn.* 95(9–11), 1384–1399 (2007). DOI: [10.1016/j.jweia.2007.02.005](https://doi.org/10.1016/j.jweia.2007.02.005).
- [31] A.M. Aly, “Atmospheric boundary-layer simulation for the built environment: Past, present and future,” *Build. Environ.* 75, 206–221 (2014). DOI: [10.1016/j.buildenv.2014.02.004](https://doi.org/10.1016/j.buildenv.2014.02.004).
- [32] M.J. Churchfield, S. Lee, J. Michalakes, and P.J. Moriarty, “A numerical study of the effects of atmospheric and wake turbulence on wind turbine dynamics,” *J. Turbul.* 13, N14 (2012). DOI: [10.1080/14685248.2012.668191](https://doi.org/10.1080/14685248.2012.668191).
- [33] R. Stoll, J.A. Gibbs, S.T. Salesky, W. Anderson, and M. Calaf, “Large-eddy simulation of the atmospheric boundary layer,” *Bound Layer Meteorol.* 177(2–3), 541–581 (2020). DOI: [10.1007/s10546-020-00556-3](https://doi.org/10.1007/s10546-020-00556-3).
- [34] R. Longo, M. Ferrarotti, C.G. Sánchez, M. Derudi, and A. Parente, “Advanced turbulence models and boundary conditions for flows around different configurations of ground-mounted buildings,” *J. Wind Eng. Ind. Aerodyn.* 167, 160–182 (2017). DOI: [10.1016/j.jweia.2017.04.015](https://doi.org/10.1016/j.jweia.2017.04.015).
- [35] A. Parente, C. Gorié, J. van Beeck, and C. Benocci, “A comprehensive modelling approach for the neutral atmospheric boundary layer: Consistent inflow conditions, wall function and turbulence model,” *Bound Layer Meteorol.* 140(3), 411–428 (2011). DOI: [10.1007/s10546-011-9621-5](https://doi.org/10.1007/s10546-011-9621-5).
- [36] M. Balogh, A. Parente, and C. Benocci, “RANS simulation of ABL flow over complex terrains applying an Enhanced k- ϵ model and wall function formulation: Implementation and comparison for fluent and OpenFOAM,” *J. Wind Eng. Ind. Aerodyn.* 104–106, 360–368 (2012). DOI: [10.1016/j.jweia.2012.02.023](https://doi.org/10.1016/j.jweia.2012.02.023).
- [37] D. Galway, J. Etele, and G. Fusina, “Development and implementation of an urban wind field database for aircraft flight simulation,” *J. Wind Eng. Ind. Aerodyn.* 103, 73–85 (2012). DOI: [10.1016/j.jweia.2012.02.010](https://doi.org/10.1016/j.jweia.2012.02.010).
- [38] G.H. Gaonkar, “Review of turbulence modeling and related applications to some problems of helicopter flight dynamics,” *J. Am. Helicopter Soc.* 53(1), 87–107 (2008). DOI: [10.4050/JAHS.53.87](https://doi.org/10.4050/JAHS.53.87).
- [39] M. Fluck, and C. Crawford, “Fast analysis of unsteady wing aerodynamics via stochastic models,” *AIAA J.* 55(3), 719–728 (2016). DOI: [10.2514/1.J054983](https://doi.org/10.2514/1.J054983).
- [40] R.E. McFarland, and K. Duisenberg, “Simulation of rotor blade element turbulence,” NASA Tech. Memo. 108862 (1995).
- [41] H. Ji, R. Chen, and P. Li, “Analysis of helicopter handling quality in turbulence with recursive von Kármán model,” *J. Aircr.* 54(5), 1631–1639 (2017). DOI: [10.2514/1.C034189](https://doi.org/10.2514/1.C034189).

- [42] H. Ji, R. Chen, L. Lu, and M.D. White, “Pilot workload investigation for rotorcraft operation in low-altitude atmospheric turbulence,” *Aerosp. Sci. Technol.* 111, 106567 (2021). DOI: [10.1016/j.ast.2021.106567](https://doi.org/10.1016/j.ast.2021.106567).
- [43] D.S. Nithya, G. Quaranta, V. Muscarello, AND M. Liang, “Review of wind flow modelling in urban environments to support the development of urban air mobility,” *Drones* 8(4) (2024). DOI: [10.3390/drones8040147](https://doi.org/10.3390/drones8040147).
- [44] A. Mohamed, M. Marino, S. Watkins, J. Jaworski, and A. Jones, “Gusts encountered by flying vehicles in proximity to buildings,” *Drones* 7(1) (2023). DOI: [10.3390/drones7010022](https://doi.org/10.3390/drones7010022).
- [45] B.J. Jonkman, *Turbsim user’s guide: Version 1.50*. National Renewable Energy Laboratory, Colorado, 2009. DOI: [10.2172/965520](https://doi.org/10.2172/965520).
- [46] P.J. Moriarty, W.E. Holley, and S.P. Butterfield, *Extrapolation of extreme and fatigue loads using probabilistic methods*, National Renewable Energy Laboratory, Colorado, 2004. DOI: [10.2172/15011693](https://doi.org/10.2172/15011693).
- [47] K.M. Kecskeny, and J.J. McNamara, “Influence of wake effects and inflow turbulence on wind turbine loads,” *AIAA J.* 49(11), 2564–2576 (2011). DOI: [10.2514/1.J051095](https://doi.org/10.2514/1.J051095).
- [48] B.F. Ng, R. Palacios, and J.M.R. Graham, “Model-based aeroelastic analysis and blade load alleviation of offshore wind turbines,” *Int. J. Control* 90(1), 15–36 (2017). DOI: [10.1080/00207179.2015.1068456](https://doi.org/10.1080/00207179.2015.1068456).
- [49] S. Baisthakur, and B. Fitzgerald, “Physics-Informed Neural Network surrogate model for bypassing Blade Element Momentum theory in wind turbine aerodynamic load estimation,” *Renew. Energy* 224, 120122 (2024). DOI: [10.1016/j.renene.2024.120122](https://doi.org/10.1016/j.renene.2024.120122).
- [50] K.-H. Kim, M. Bertelè, and C.L. Bottasso, “Wind inflow observation from load harmonics via neural networks: A simulation and field study,” *Renew. Energy* 204, 300–312 (2023). DOI: [10.1016/j.renene.2022.12.051](https://doi.org/10.1016/j.renene.2022.12.051).
- [51] Z.J. Chen, K.A. Stol, and P.J. Richards, “Preliminary design of multirotor UAVs with tilted-rotors for improved disturbance rejection capability,” *Aerosp. Sci. Technol.* 92, 635–643 (2019). DOI: [10.1016/j.ast.2019.06.038](https://doi.org/10.1016/j.ast.2019.06.038).
- [52] M. Bahr, E. Ferede, and F. Gandhi, “Flight characteristics of AAM/UAM-scale Quadcopters under atmospheric turbulence,” in *Vertical Flight Society’s 78th Annual Forum & Technology Display*, Fort Worth, TX, 2022.

- [53] T. Noboni, J. McConnell, and T. Das, “Altitude control of a tethered multi-rotor autogyro in 2-D using pitch actuation via differential rotor braking,” in American Control Conference (ACC), San Diego, CA, 2023: pp. 2848–2854. DOI: [10.23919/ACC55779.2023.10155811](https://doi.org/10.23919/ACC55779.2023.10155811).
- [54] T. Noboni. Altitude and pitch control of a tethered multi-rotor autogyro using a reduced order model. University of Central Florida, FL, 2024.
- [55] L.D. Milfont, G.T. de Carvalho Ferreira, and M. Giesbrecht, “Fault diagnosis in electric machines and propellers for electrical propulsion aircraft: A review,” *Eng. Appl. Artif. Intell.* 139, 109577 (2025). DOI: [10.1016/j.engappai.2024.109577](https://doi.org/10.1016/j.engappai.2024.109577).
- [56] M.S. Araghizadeh, B. Sengupta, H. Lee, and R.S. Myong, “Aeroacoustic investigation of side-by-side urban air mobility aircraft in full configuration with ground effect,” *Phys. Fluids* 36(8), 87160 (2024). DOI: [10.1063/5.0221902](https://doi.org/10.1063/5.0221902).
- [57] R. Heinrich, and L. Reimer, “Comparison of different approaches for gust modeling in the CFD Code TAU,” in International Forum on Aeroelasticity and Structural Dynamics, Bristol, UK, 2013. <https://elib.dlr.de/85834/>.
- [58] J. Müller, T. Lutz, and E. Krämer, “Numerical simulation of the swept FNG wing in atmospheric turbulence,” 2020. DOI: [10.2514/6.2020-2778](https://doi.org/10.2514/6.2020-2778).
- [59] H. Lee, and D.-J. Lee, “Low Reynolds number effects on aerodynamic loads of a small scale wind turbine,” *Renew. Energy* 154, 1283–1293 (2020). DOI: [10.1016/j.renene.2020.03.097](https://doi.org/10.1016/j.renene.2020.03.097).
- [60] B. Sengupta, Y. Lee, M.S. Araghizadeh, R.S. Myong, and H. Lee, “Comparative analysis of direct method and fast multipole method for multicopter wake dynamics,” *Int. J. Aeronaut. Space Sci.* 25(3), 789–808 (2024). DOI: [10.1007/s42405-023-00699-w](https://doi.org/10.1007/s42405-023-00699-w).
- [61] B. Sengupta, E. Esmailifar, M. Sadegh Araghizadeh, S. Kang, H. Lee, R.S. Myong, and L.P. Prince Raj, “Rotor-fuselage-intake aerodynamics and icing using vortex and eulerian–Lagrangian computational fluid dynamics methods,” *AIAA J.* 63(3), 1–22 (2025). DOI: [10.2514/1.J064813](https://doi.org/10.2514/1.J064813).
- [62] J. Katz, and A. Plotkin. Low-speed aerodynamics. Cambridge University Press, Cambridge, 2001.
- [63] H. Lee, B. Sengupta, M.S. Araghizadeh, and R.S. Myong, “Review of vortex methods for rotor aerodynamics and wake dynamics,” *Adv. Aerodyn.* 4(1), 20 (2022). DOI: [10.1186/s42774-022-00111-3](https://doi.org/10.1186/s42774-022-00111-3).
- [64] K.S. Brentner, “Prediction of helicopter rotor discrete frequency noise for three scale models,” *J. Aircr.* 25(5), 420–427 (1988). DOI: [10.2514/3.45598](https://doi.org/10.2514/3.45598).

- [65] N. Kelley, and B. Jonkman, TurbSim stochastic inflow turbulence simulator, National Renewable Energy Laboratory, Colorado, 2012. <https://www2.nrel.gov/wind/nwtc/turbsim>.
- [66] N.D. Kelley, and B.J. Jonkman, Overview of the Turbsim stochastic inflow turbulence simulator, National Renewable Energy Laboratory, Colorado, 2005.
- [67] C. Dyrbye, and S.O. Hansen, Wind loads on structures, Wiley and Sons, New York, 1997. <https://archive.org/details/windloadsonstruc0000dyrb/page/24/mode/2up?q=Power+law+exponent+>.
- [68] Beal, T. R., "Digital Simulation of Atmospheric Turbulence for Dryden and von Karman Models," *Journal of Guidance, Control, and Dynamics*, Vol. 16, No. 1, 1993, pp. 132–138. DOI: [10.2514/3.11437](https://doi.org/10.2514/3.11437)
- [69] Liu, X., Abà, A., Capone, P., Manfredi, L., and Fu, Y., "Atmospheric Disturbance Modelling for a Piloted Flight Simulation Study of Airplane Safety Envelope over Complex Terrain," *Aerospace*. 2. Volume 9. DOI: [10.3390/aerospace9020103](https://doi.org/10.3390/aerospace9020103)
- [70] M. Somoano, T. Battistella, A. Rodríguez-Luis, S. Fernández-Ruano, and R. Guanche, "Influence of turbulence models on the dynamic response of a semi-submersible floating offshore wind platform," *Ocean Eng.* 237, 109629 (2021). DOI: [10.1016/j.oceaneng.2021.109629](https://doi.org/10.1016/j.oceaneng.2021.109629).
- [71] S. Bhattacharya, L. Arany, J. Macdonald, and S. Hogan, "Simplified critical mudline bending moment spectra of offshore wind turbine support structures," *Wind Energy* 18 (2014). DOI: [10.1002/we.1812](https://doi.org/10.1002/we.1812).
- [72] W.J. Devenport, J.K. Staubs, and S.A.L. Glegg, "Sound radiation from real airfoils in turbulence," *J. Sound Vib.* 329(17), 3470–3483 (2010). DOI: [10.1016/j.jsv.2010.02.022](https://doi.org/10.1016/j.jsv.2010.02.022).
- [73] Y.Y. Dang, G.H. Gaonkar, and J.V.R. Prasad, "Parallel methods for turbulence simulation and helicopter-response prediction," *J. Am. Helicopter Soc.* 41(3), 219–231 (1996). DOI: [10.4050/JAHS.41.219](https://doi.org/10.4050/JAHS.41.219).
- [74] H. Ji, R. Chen, and P. Li, "Real-time simulation model for helicopter flight task analysis in turbulent atmospheric environment," *Aerosp. Sci. Technol.* 92, 289–299 (2019). DOI: [10.1016/j.ast.2019.05.066](https://doi.org/10.1016/j.ast.2019.05.066).
- [75] B. Litherland, and S. Holland, NASA urban air mobility (UAM) reference vehicles, National Aeronautics and Space Administration, Colorado, 2023. <https://sacd.larc.nasa.gov/uam-refs/>.
- [76] C. Silva, and W. Johnson, "Practical conceptual design of quieter urban VTOL aircraft," in 77th Annual Forum. Vertical Flight Society, vols. 11–13, 2021.
- [77] P. Ventura Diaz, W. Johnson, J. Ahmad, and S. Yoon, "Computational study of the side-by-side urban air taxi concept," in Vertical Flight Soc.'s (VFS) Annual Forum and Technology Display, Philadelphia, PA, US, 2019.

- [78] W. Johnson, Rotorcraft aeromechanics, Cambridge University Press, Cambridge, 2013. DOI: [10.1017/CBO9781139235655](https://doi.org/10.1017/CBO9781139235655).
- [79] I. Chopra, and A. Datta, "Helicopter dynamics," ENAE (2011).
- [80] W. Johnson, C. Silva, and E. Solis, "Concept vehicles for VTOL air taxi operations," in AHS Technical Conference on Aeromechanics Design for Transformative Vertical Flight, San Francisco, CA, 2018.
- [81] J.G. Leishman, Introduction to aerospace flight vehicles, Embry-Riddle Aeronautical University – Daytona Beach, FL, 2023. DOI: [10.15394/eaglepub.202](https://doi.org/10.15394/eaglepub.202).
- [82] N. André, and M. Hajek, "Robust environmental life cycle assessment of electric VTOL concepts for urban air mobility," in AIAA Aviation 2019 Forum, Dallas, TX, 2019. <https://doi.org/doi:10.2514/6.2019-3473>.
- [83] C. Silva, W.R. Johnson, E. Solis, M.D. Patterson, and K.R. Antcliff, "VTOL urban air mobility concept vehicles for technology development," in Aviation Technology, Integration, and Operations Conference. American Institute of Aeronautics and Astronautics; Reston, Virginia, vol. 3847, 2018. DOI: [10.2514/6.2018-3847](https://doi.org/10.2514/6.2018-3847).
- [84] Z. Zhang, L. Liu, Y. Shi, K. Zhang, K. Liu, S. Wang, and F. Hu, "Analysis of urban turbulence intensity observed by Beijing 325-m tower and comparison with the IEC turbulence model for small wind turbines," J. Wind Eng. Ind. Aerodyn. 241, 105511 (2023) (2023). DOI: [10.1016/j.jweia.2023.105511](https://doi.org/10.1016/j.jweia.2023.105511).
- [85] M. Rotach, Turbulence within and above an URBAN canopy, ETH Zürich, Zurich, 1991.
- [86] Pérez Albornoz, C., Escalante Soberanis, M. A., Ramírez Rivera, V., and Rivero, M., "Review of Atmospheric Stability Estimations for Wind Power Applications," *Renewable and Sustainable Energy Reviews*, Vol. 163, 2022, p. 112505. DOI: [10.1016/j.rser.2022.112505](https://doi.org/10.1016/j.rser.2022.112505)
- [87] Inc. Tecplot, User's Manual Tecplot 360 2024 Release 1 (2024).
- [88] Lawson, M. V, "Progress towards Quieter Civil Helicopters," *The Aeronautical Journal*, Vol. 96, No. 956, 1992, pp. 209–223. DOI: [10.1017/S0001924000050508](https://doi.org/10.1017/S0001924000050508)
- [89] Paterson, R. W., and Amiet, R. K., "Noise of a Model Helicopter Rotor Due to Ingestion of Turbulence," 1979.
- [90] J. Lee, K. Yee, and S. Oh, "Aerodynamic characteristic analysis of multi-rotors using a modified free-wake method," *Trans. Jpn. Soc. Aeronaut. Space Sci.* 52(177), 168–179 (2009). DOI: [10.2322/tjsass.52.168](https://doi.org/10.2322/tjsass.52.168).
- [91] R. Healy, J. McCauley, F. Gandhi, and O. Sahni, "A computational examination of side-by-side rotors in ground effect," *J. Am. Helicopter Soc.* 68(3), 32007–32024 (2023). DOI: [10.4050/JAHS.68.032007](https://doi.org/10.4050/JAHS.68.032007).

